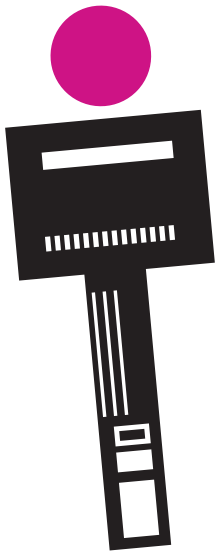

RAM ROBOTICS AND MECHATRONICS

MDR

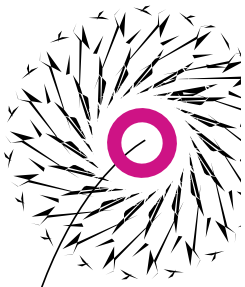

ENHANCING ROBOTIC PRECISION IN MRI-GUIDED ABDOMINAL INTERVENTIONS USING ACTIVE TRACKING

M. (Mitchel) Doets

MSC ASSIGNMENT

Committee:
dr. ir. M. Abayazid
dr. V. Groenhuis, MSc
dr. ir. K. Niu
dr. ir. W.M. Brink

February, 2025

010RaM2025
Robotics and Mechatronics
EEMCS
University of Twente
P.O. Box 217
7500 AE Enschede
The Netherlands

UNIVERSITY OF TWENTE. | TECHMED CENTRE

UNIVERSITY OF TWENTE. | DIGITAL SOCIETY INSTITUTE

Abstract

Early-stage cancer diagnosis is crucial for improving survival rates. Biopsy is the most common diagnostic method and image guidance can be used to enhance such a biopsy. MRI-guided biopsies enable the targeting of small liver lesions that are not visible using ultrasound US or CT. However, the widespread adoption of MRI-guided biopsies is limited due to workflow inefficiencies, particularly for dynamic abdominal targets, where accurate needle placement remains challenging.

This thesis introduces a new developed Manipulator Arm for MRI (MAMRI), which is a pneumatic stepper motor driven six degree of freedom MR-safe robotic arm to accurately position a needle and follow a dynamic lesion. The robotic device is integrated with active tracking on MRI to asses how active MR-tracking can be used to characterize and enhance the kinematic performance of MAMRI.

Two interchangeable end-effectors were developed to support a manual needle injection procedure and a motorized procedure. An analytical approach was used within a kinematic model to actuate MAMRI and to calculate a predicted location for the needle tip using forward kinematics. An active tracking sequence was used to track RF microcoils in 3D at 21.53 fps. A software interface (Access-I) was used to remotely process projection data acquired to position data with a spatial resolution of 0.78 mm. A graphical user interface (GUI) was developed to control MAMRI and execute Python-coded protocols. The quality and consistency of the position data, including angle dependency, were analyzed. The Euclidean distance was used to evaluate errors between the RF microcoil on the surrogate needle tip, the virtual target, and the RF microcoil representing surrogate anatomy.

Both static and dynamic performance of MAMRI were evaluated. The motorized end-effector successfully actuated the needle, and the kinematic model effectively predicted and assessed MAMRI's kinematic performance. A mean accuracy of 2.83 $\pm$ 0.78 mm was achieved when targeting a static lesion. However, improvements in dynamic performance are needed, particularly by reducing the observed delay between the surrogate needle tip and the surrogate anatomical path.

This research marks an initial step toward implementing real-time MRI active tracking using RF microcoils to enhance and evaluate MAMRI's performance in MR-guided abdominal biopsies. The results suggest that this offers significant potential advantages for MR-guided interventions, potentially enhancing accuracy in targeting abdominal lesions, clinical workflow and ultimately leading to better clinical outcomes. This could contribute to improved abdominal cancer diagnosis.

Samenvatting

Vroegtijdige kanker diagnose is een van de belangrijkste dingen in het verbeteren van overlevingskansen. Biopsie is de meest standaard methode voor zulke diagnoses en beeldgeleiding kan zo een interventie nauwkeuriger maken. Een MRI begeleide biopsie maakt het mogelijk leverlaesies te biopteren, die op Echo en CT niet zichtbaar zijn. Echter is grootschalige toepassing beperkt door inefficiënties in de workflow, vooral bij dynamische abdominale doelen blijft nauwkeurige naald plaatsing een uitdaging.

Deze thesis introduceert de Manipulator Arm voor MRI (MAMRI), een nieuw ontwikkelde MR-Safe robotarm met zes vrijheidsgraden (6-DOF), aangedreven door pneumatische stappenmotoren. MAMRI is ontworpen om een biopsienaald nauwkeurig te positioneren en een dynamische laesie in real-time te volgen. Dit robotsysteem is geïntegreerd met actieve MRI-tracking om te onderzoeken hoe real-time MR-tracking kan worden gebruikt om de kinematische prestaties van MAMRI te karakteriseren en te verbeteren.

Twee verwisselbare end-effectors zijn ontwikkeld om zowel een handmatige naaldinjectie als een gemotoriseerde naaldinjectie te ondersteunen. Een analytische benadering werd gebruikt binnen een kinematisch model om MAMRI aan te sturen en de verwachte positie van de naaldtip te berekenen met behulp van forward kinematics. Een actieve trackingsequentie werd toegepast om RF microcoils in 3D te volgen met 21.53 fps, waarbij de spatial resolution 0.78 mm bedroeg. Een software-interface (Access-I) werd gebruikt om de projectiegegevens te verwerken tot positiedata. Daarnaast werd een grafische gebruikersinterface (GUI) ontwikkeld om MAMRI te besturen en Python-gecodeerde protocollen uit te voeren. De kwaliteit en consistentie van de positiedata, inclusief hoekafhankelijkheid, werden geanalyseerd. De Euclidische afstand werd gebruikt om errors te bepalen tussen de RF microcoil gefixeerd op de surogaat naaldpunt, het virtuele doel, en de RF microcoil die de surrogaat anatomie vertegenwoordigt.

Zowel de statische als dynamische prestaties van MAMRI werden geëvalueerd. De gemotoriseerde end-effector kon de naald succesvol aansturen, en het kinematische model kon effectief de prestaties van MAMRI voorspellen en evalueren. Een gemiddelde nauwkeurigheid van 2.83 $\pm$ 0.78 mm werd gemeten voor het bereiken van een statische laesie. Verbeteringen in de dynamische prestaties zijn echter noodzakelijk, met name door het verminderen van de waargenomen vertraging tussen de positie van de naald punt en het doelwit.

Dit onderzoek vormt een eerste stap in de implementatie van real-time MRI-actieve tracking met RF microcoils om de prestaties van MAMRI bij MR-geleide abdominale biopsies te verbeteren en te evalueren. De resultaten suggereren dat deze aanpak aanzienlijke voordelen kan bieden voor MRI-geleide interventies, zoals verbeterde nauwkeurigheid, klinische workflows en uiteindelijk betere klinische uitkomsten. Dit kan bijdragen aan een verbeterde diagnose van abdominale kanker.

Contents

1 Introduction

One out of five people will develop a form of cancer during their lifetime, more than 25% of these cancers are located in the abdomen [1]. Diagnosing such cancers within an early stage is crucial for survival rates [2]. The most common method of diagnosing cancer is biopsy. Due to the substantial overlap between the representation of diseases on a clinical and radiological level, a pathological investigation of the conspicuous tissue (lesion) sample is needed to determine the appropriate diagnosis and treatment. Medical imaging can be used to locate such a lesion and guide a biopsy needle towards the target. The use of magnetic resonance imaging (MRI) provides the capability to detect abdominal lesions that may not be visible with other conventional imaging modalities, such as computed tomography (CT) and ultrasound (US). Additionally, MRI offers advantages like the absence of ionizing radiation, multi-planar scanning, excellent ratios of soft tissue contrast, and spatial resolution [3]. Research suggests that the use of MRI guidance for a biopsy has the potential to double the accuracy of the procedure compared to CT guidance [4]. The use of real-time MRI guidance has been shown to enable higher success rates and lower complication rates in diagnostic biopsy procedures of small liver lesions (<20 mm). In contrast, such lesions would not even be visible on US [4].

Despite the potential of MRI, the large-scale acceptance is hampered by MRI occupation time and the limited space available around the patient in a conventional horizontal bore system. The needle placement process is time-consuming and inefficient. Procedures often involve moving the patient out of the bore multiple times to gradually move the needle towards the target lesion. This workflow is particularly challenging for dynamic targets within the abdomen, which are subject to move upon respiration. Additionally, the target lesion deforms under the influence of the pressure of the needle on the tissue. This increases the complexity and duration of accurate needle placement, potentially resulting in inaccurate biopsies and leading to incorrect diagnosis.

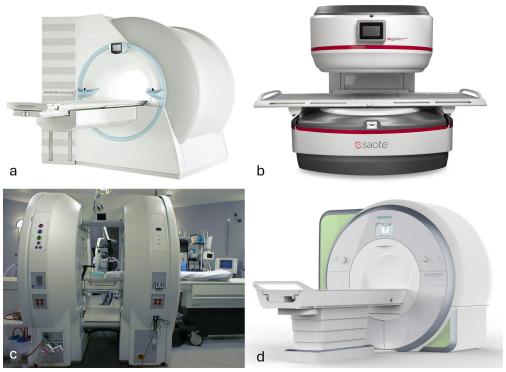

Figure 1.1: Overview of four different types of MR scanners:(a) Symphony (Siemens Healthineers, Erlangen, Germany) a closed 60 cm bore (1.5T) scanner with a length of 160 cm [5]. (b) Magnifico (Esaote, Genoa, Italy) an open bore (0.4T) scanner [6]. (c) Signa SP (General Electric, Boston, United States of America) a double-doughnut design [7]. (d) Aera (Siemens Healthineers, Erlangen, Germany) a 70 cm bore (1.5T) scanner with a length of 145 cm [8].

1.1 Interventional MRI

In the last two decades, many attempts have been made to improve the workflow of these kinds of MR-guided procedures, for instance, by increasing patient reachability by increasing the openness of MRI systems. Various MRI configurations (Figure 1.1) have been developed, such as open-bore designs with permanent magnets with lower field strengths (0.2-1 T), increased cylindrical bore sizes (70+ cm) and a double doughnut-shaped system (General Electric, Boston, United stated of America) where the middle of the bore was cut-out, leading to a split cylindrical design to increase patient access for intervention. However, these configurations encounter an important trade-off [9]. High-quality MR Imaging relies on factors such as magnetic field homogeneity, strength and stability. These factors are best met by prioritizing closed magnet configurations such as a spherical magnet. However, interventional use of MRI requires an open system, which often compromises image quality. The

Figure 1.2: Robotic manipulators to enhance an MR-guided biopsy: (a) Sunram 7 (University of Twente, Enschede, Netherlands) for breast [11] (b) Remote controlled Manipulator (Soteria Medical, Arnhem, Netherlands) for prostate [10] (c) MIRIAM (University of Twente, Enschede, Netherlands) for prostate [12]. (d) Innomotion (Innomedic, Herxheim, Germany) for abdominal [13]. (e) GantryMate (Interventional Systems, Kitzbühel, Austria) for abdominal [14].

Signa SP was discontinued due to high production costs and poor image quality. Although open magnet designs future field strengths close to the diagnostic standard of 1.5T field strength, the performance and capabilities of these systems cannot compete with the state-of-the-art cylindrical horizontal bore systems with a bore of 70 cm, which is the current conventional standard [10].

Parallel to the evolution of MRI technology, the development of tools to perform interventional procedures remotely has advanced significantly, particularly in fields such as prostate, breast and brain interventions. These systems face specific challenges in actuation due to the constraints imposed by the MRI environment. Conventional electrical motors are generally not MRI-compatible due to the incorporation of permanent magnets, as these magnetic components interfere with MRI signals, degrade image quality, and are subject to strong attractive forces from the scanner's magnetic field.

1.2 Robotics for MRI Interventions

The Sunram 7 MR-safe breast biopsy robot, developed at the University of Twente (Robotics and Mechatronics, Enschede, Netherlands), consists of five pneumatic stepper motors that drive a biopsy needle towards a lesion in the breast. It achieves an in-plane accuracy of 1.72 ± 0.84 mm with five degrees of freedom (DOF) [11], as shown in Figure 1.2. Soteria medical (Arnhem, Netherlands) brought a 5-DOF MR-Safe robot on the market actuated by pneumatic motors, which can be directed from the control room to guide a prostate biopsy [10]. Several robotic approaches have been developed that are based on piezoelectric motors, being MR-conditional, such as the MIRIAM Robot (also developed at the University of Twente) with 4 DOF for prostate biopsies [12]. Innomotion (Innomedic, Herxheim, Germany) is known as a 6-DOF robot for percutaneous MR interventions driven by piezo-electric motors with an accuracy of up to millimetres but was redesigned to pneumatic actuation when it was discovered that the presence of piezoelectric components could introduce disturbances to the MRI signal, such as eddy currents and a reduction in signal-to-noise ratio (SNR) [13]–[15]. These negative effects induced by the presence of these piezoelectric components was also seen in the robot's mentioned above [12]. Within GantryMate (Interventional Systems, Kitzbühel, Austria), a 4 DOF patient-mounted robot, these effects are tried to be minimized by placing the piezoelectric motors at the feet of the patient, steering the robot by Bowden cables [14]. This robot uses passive MR tracking to align a marker attached to the needle guide with the lesion on the image, improving the accuracy to 1.7 ± 1.0 mm.

Although these robotic tools show potential to enhance MR-guided interventions, several limitations persist. Pneumatic actuation can lack precision due to missed steps or insufficient force [16]. The Innomotion system was discontinued due to its limited adaptability and cost-effectiveness [14]. Bowden cables used to mitigate the negative effects of piezoelectric signals on MRI still do not result in robotic systems being fully MR-safe.

Other robotic approaches, such as those using magnetic resonance-controlled actuation, hydraulics, and soft actuation, also present challenges. Magnetic resonance-controlled actuation

generates low torques [17]. Hydraulic actuation can produce higher forces but is often slow, complex, and prone to maintenance issues due to potential leaks. Soft actuation systems, though lightweight and flexible, typically offer low force output and limited precision [17].

These challenges necessitate application-specific designs, limiting versatility and cost-effectiveness. This thesis focuses on developing a versatile and MR-safe robotic platform with the potential to be used for a wide range of MR-guided interventions.

1.3 Real-time MRI

Recent advances in data acquisition techniques have enabled real-time MRI guidance [18]. An important trade-off has to be made between temporal and spatial resolution, which are intertwined with signal-to-noise ratio, in order to image dynamic processes. An increase in temporal resolution, which is inversely proportional to the frame rate, would demand a smaller latency and reconstruction time [18]. MRI guidance is typically based on 2D imaging techniques such as balanced steady-state free precession (bSSFP), single-shot Fast Spin Echo (HASTE/SS-FSE) or non-Cartesian sampling [19]. However, multiple slices are needed to monitor out-of-plane movement and adjust the scan plane accordingly. Typically, up to three slices, either orthogonal or parallel, are used to minimize processing time [18]. To adjust the scan-plane during real-time scanning image processing tools have been suggested (passive tracking) to follow the moving object (lesion, needle) [18]. Such an algorithm would enable closed-loop confirmation of needle placement [20]. A Mask Region-Based Convolutional Neural Network (Mask R-CNN) has been proposed for fast object detection and segmentation [20]. However, these algorithms face challenges due to the obliqueness of the needle relative to the scan planes and discrepancies between the needle's appearance in MRI and its actual physical position [21].

The use of Model-based Reconstruction of MOTion from Undersampled Signal (MR-MOTUS) is one of the uprising techniques to reconstruct 3D motion directly from k-space data [22]. This technique can potentially estimate motion without direct restriction from the temporal resolution of imaging. Another emerging technique is live-view golden-angle radial sparse parallel (GRASP) [23], this technique consists of two phases: In the off-view phase a 4D (3D + time) database is acquired and reconstructed, each off-view 3D image is coupled to a 2D image used as a navigator. In the live-view phase only 2D images are required, these are matched to the 2D navigator, which is then linked to a 3D motion estimation [23].

Three-dimensional (3D) motion information of the abdominal lesion and the biopsy needle is promising for enhancing the accuracy of MR-guided biopsies. However, when the needle and lesion are not aligned within the same imaging plane, it becomes challenging to obtain this information using the readily available two-dimensional (2D) real-time MR imaging techniques. Alternative methods based on 'active tracking' avoid the need for 2D or 3D image reconstruction and analysis altogether, enabling the possibility of tracking non-anatomical objects.

1.4 Active tracking

Active tracking offers an alternative to image-based approaches by using radiofrequency (RF) microcoils. These coils detect MR signal frequencies that are encoded to their 3D positions. With tracking rates of up to 50 fps, active tracking enables the real-time monitoring of multiple RF microcoils simultaneously in 3D. This approach achieves higher spatial and temporal resolution compared to passive tracking [24], [25].

Placing RF microcoils on a robotic system designed for needle placement within an MRI environment enables real-time evaluation of the robotic performance and needle positioning. This facilitates continuous feedback, making real-time adjustments to correct any misalignment along the intended injection path possible.

1.5 Research Goal

This thesis focuses on implementing active MR-tracking using RF microcoils on a newly developed MR-safe manipulator arm for MRI (MAMRI), Figure 1.3. MAMRI is designed by V. Groenhuis and builds upon the successes of the Sunram breast biopsy robots [11]. Coming with six pneumatically driven degrees of freedom, it offers more flexibility than the state-of-the-art MR robotic solutions, being developed to be versatile for a range of MR-guided interventions and tailored specifically for this project.

The primary objectives of this research include:

1. Determining the required dimensions and configuration of MAMRI for abdominal applications. (Section 2.1)
2. Developing a kinematic model for the MAMRI system. (Section 3.2)
3. Designing and fabricating two interchangeable end-effectors: a needle guide and a pneumatically actuated needle placement system. (Section 3.1.1)
4. Developing a universally compatible baseplate for securing setups to a Siemens MR scanner bed. (Section 3.1.2)
5. Developing an algorithm for localizing RF microcoils inside MRI. (Section 3.3)
6. Developing a graphical user interface (GUI) to control the robot and provide real-time visualization of the RF microcoil positions and robotic movements. (Section 3.4.1)
7. Evaluation of the quality of RF microcoil position information. (Chapter 4)
8. Assessing the robot's movement and accuracy by targeting both stationary and dynamic targets. (Chapter 4)

These objectives address the central research question:

How can active MR-tracking be used to characterize and enhance the performance of the 6-DOF pneumatic MR-safe manipulator arm for MRI (MAMRI)?

To simulate a (moving) target lesion, an RF microcoil is used as a surrogate for anatomical structures. This approach offers the advantage of decoupling robotic performance and setpoint information from the quality and temporal resolution of MR image-based tracking. Additionally, it allows for obtaining both the target position and the position of the RF microcoil placed on the robot using one single method (active tracking) with comparable accuracy.

The RF microcoil on MAMRI is fixed to a surrogate needle and placed into the designed end-effector to facilitate tracking of the needle tip without relying on a kinematic model-based approach, where the needle position would typically be calculated using an RF microcoil placed on the robotic arm. By placing the RF microcoil directly on the surrogate needle, in combination with the surrogate anatomy, the kinematic model can be rigorously evaluated to identify potential areas for system-level improvement. This is a fundamental step towards improving the performance of MAMRI using RF microcoils integrated into the robotic arm.

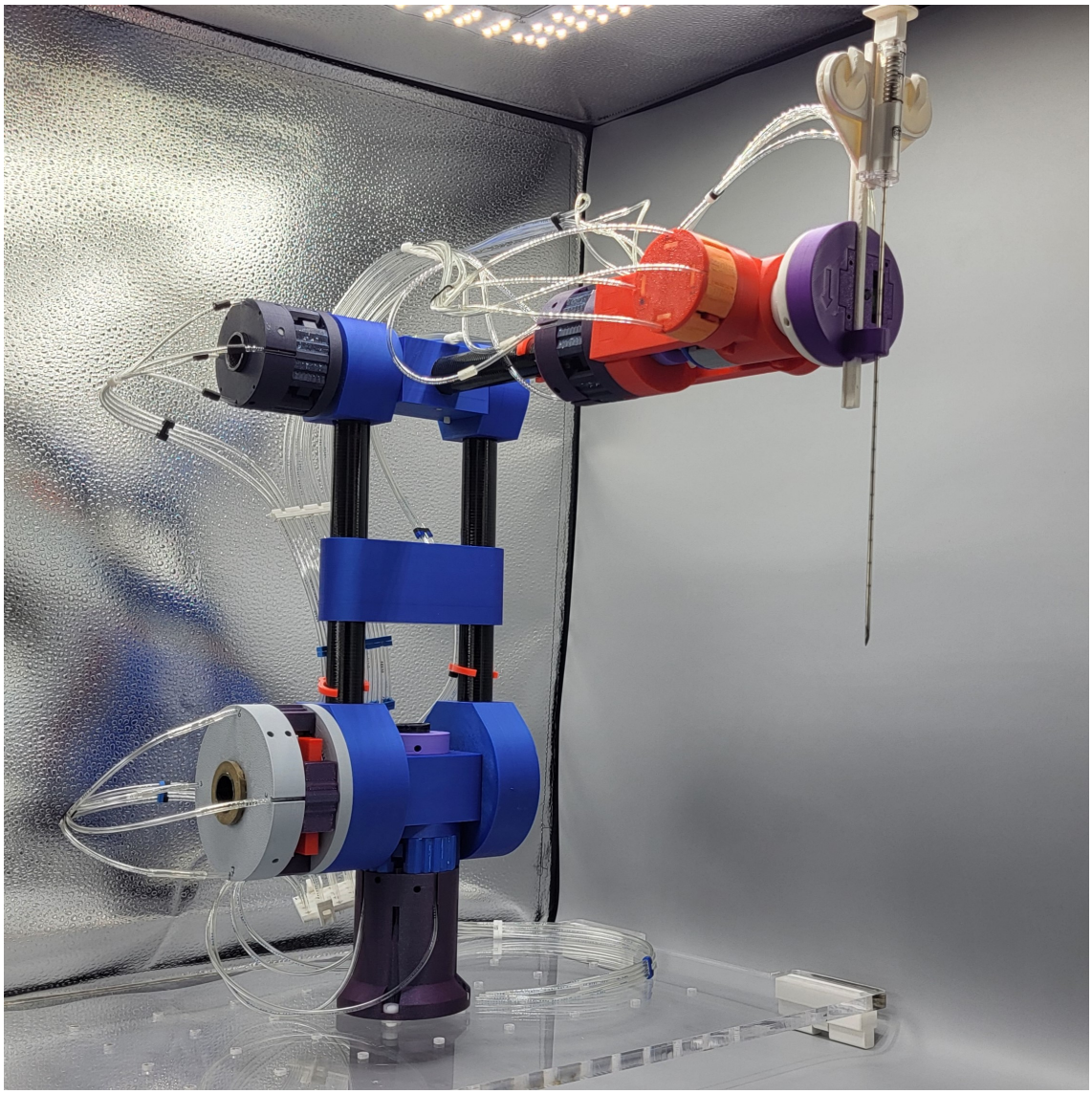

Figure 1.3: MAMRI (University of Twente, Enschede, Netherlands) an MR-safe robotic platform driven by pneumatic stepper motors designed to be versatile in MRI-guided interventions

2 Background

Within this chapter, the MAMRI robot will be further explained, and the size and configuration of the system will be evaluated in context to the abdominal application. Next to this, the background information needed for the use of active real-time MR-tracking is described.

2.1 MAMRI

The Manipulator arm for Magnetic Resonance Imaging (MAMRI) is driven by six newly designed revolute pneumatic stepper motors featuring a harmonic drive (strain wave gear reduction). This provides a higher gear ratio, higher torques and rigidity of the robotic system [26], [27]. The system is constructed from MR-safe materials, with most components being 3D-printed to facilitate rapid prototyping. This allows for tailoring motor dimensions and torque capacities to meet specific application requirements, enhancing the system's versatility.

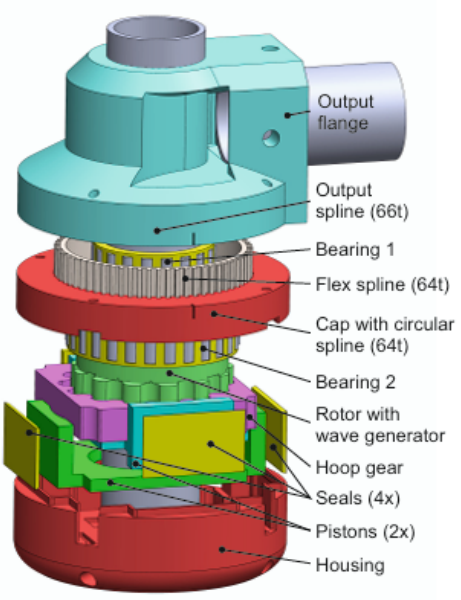

Figure 2.1: Exploded view of one of the variants of pneumatic motors used in MAMRI, featuring a harmonic drive.

For the abdominal application of MAMRI, it was regarded advantageous to have a workspace capable of reaching at least three-quarters of the length of an average patient's torso, which is approximated to a minimum workspace length of 40 cm. Additionally, to enable the needle to be actuated to any point within the bore cross-section, a cylindrical workspace was defined with a diameter of 55 cm. This dimension is defined by the internal diameter of a conventional 70 cm bore, with an added safety margin of approximately 10 millimetres to prevent collisions between MAMRI and the bore.

Various curved arm configurations were considered, designed to follow the curvature of the bore [28]. However, simulations of the kinematic models revealed that a straight-arm configuration would offer greater versatility for the defined workspace requirements. These considerations led to the development of a tailored variant of the MAMRI system used in this research, as illustrated in Figure 2.2.

The MAMRI system is positioned between the patient's legs to utilize the vertical space within the bore, allowing maximum freedom for arm actuation. The dimensions were designed such that the rotation point of the second joint (J2) is located above the patient's perineum. This placement ensures optimal rotational reach of 180 degrees (-90 to +90 degrees relative to the base position), enhancing the system's ability to reach target areas effectively.

The length of the arm segment between joint 2 (J2) and joint 3 (J3) is specifically designed to prevent collisions between the arm and the bore, as can be seen in Figure 2.3, with the exception of the end-effector, which in theory could interact with the bore but is prevented by the collision avoidance protocol covered in Section 3.4.3. This ensures optimal operation within the spatial constraints of the MRI environment. The segment length between the shoulder (J3) and the end-effector is dimensioned to allow coverage of the entire required workspace, including areas near the base and at the distal end. This prevents overextension of the arm

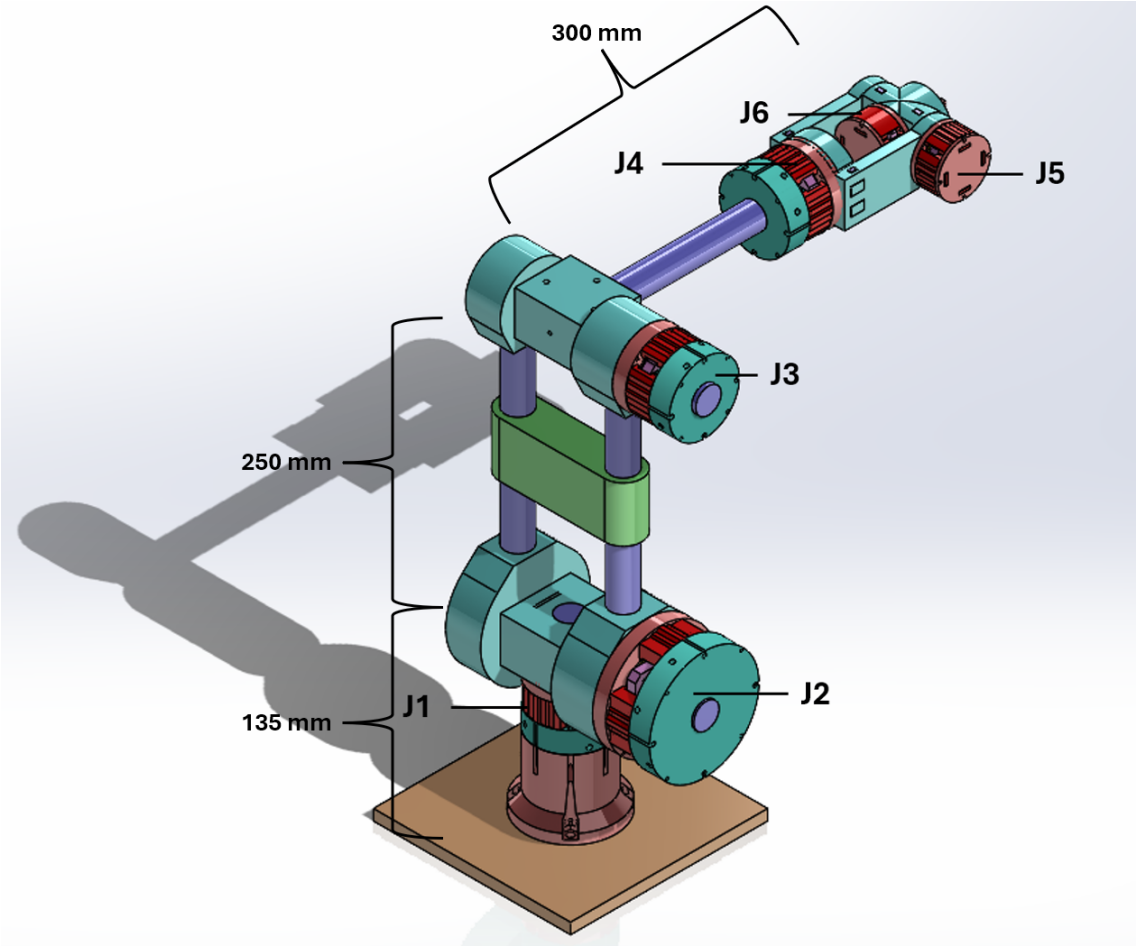

Figure 2.2: The tailored version of MAMRI, in L-shaped base configuration, used in this research with the relevant dimensions and indication of the six pneumatically driven joints

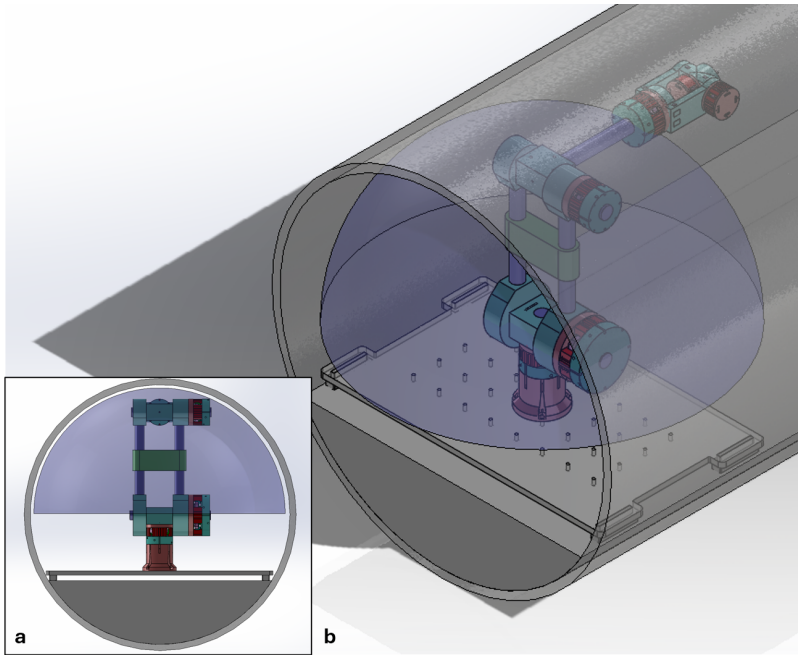

Figure 2.3: The workspace formed by joint 1 and joint 2 visualized in a 3D rendering (a), demonstrating that a collision between the bore and the arm is avoided, as there is no intersection between the workspace and the bore (b).

Table 2.1: Transmission ratios and corresponding step sizes for each joint of the MAMRI system.

Joint	Transmission Ratio	Step Size (°)
1,4	1:33	0.21
2	1:51	0.14
3	1:31	0.22
5,6	1:25	0.28

and avoids configurations where arm segments would need to collide to reach a target point, ensuring efficient operation.

The design incorporates three different sizes of joints, with the largest motors positioned near the base to provide the highest torque, while smaller motors are used for orienting the end-effector. These six motors are driven by four pneumatic tubes per motor, resulting in 24 tubes which cyclically actuate two pistons per motor. This motion drives a 14-tooth hoop gear that interacts with a 13-tooth cycloidal gear and a strain wave gear.

Each joint is equipped with a strain wave gear optimized for its specific function, providing the following transmission ratios and the resulting step sizes, table 2.1.

2.2 MAMRI controller

In earlier research, a controller has been developed to pneumatically actuate MAMRI by using multiple electrically controlled valves (Figure 2.4) [26]. These valves regulate the movement of the pistons within the stepper motors. Since this controller features 32 valves, eight motors can be driven using four tubes for each motor. For each of these motor's two buttons are present to actuate the motor independently in the positive and negative direction as defined by the kinematic model (Section 3.2). The controller can be connected to an external PC, enabling control of MAMRI according to defined protocols, such as the kinematic model outlined in Section 3.2.

2.3 Magnetic Resonance Imaging

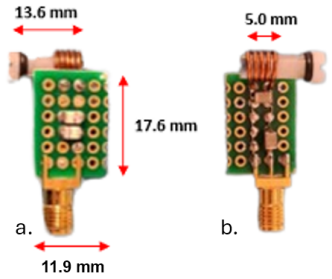

Figure 2.5: Composition of the used RF microcoils, being in-house developed [29]. The ceramic diodes are soldered on a PCB (a) (Bottom view), and the micro-coil (solenoid) is soldered next to two capacitors (b) (Top view) a small volume sample is placed inside the solenoid

MRI is based on the magnetic resonance characteristics of the nucleus of an atom. Most MRI systems use the Nuclear magnetic resonance (NMR) of hydrogen (H^1), which is a very abundant atom in the human body [30]. A strong static magnetic field is used in conjunction with switched gradient fields and radio frequency pulses to elicit a signal from the sample. Specific timing diagrams, known as pulse sequences, are used to highlight certain tissue characteristics by exploiting tissue-specific spin dynamics [30]. Conventional 2D imaging relies on spatial encoding, where the resonance frequency of a sample varies based on its position under the influence of magnetic field gradients. This process involves slice selection, followed by phase and frequency encoding. By adjusting gradient directions, images can be acquired in arbitrary orientations. Additionally, multiple slices can be stacked to create a 3D rendering of a specific cross-section [30].

2.3.1 Active real-time MR-tracking

As mentioned in the Chapter 1 the principles used in MR imaging also enable active tracking by using RF microcoils. Based on the principles of frequency encoding using a field gradient, a

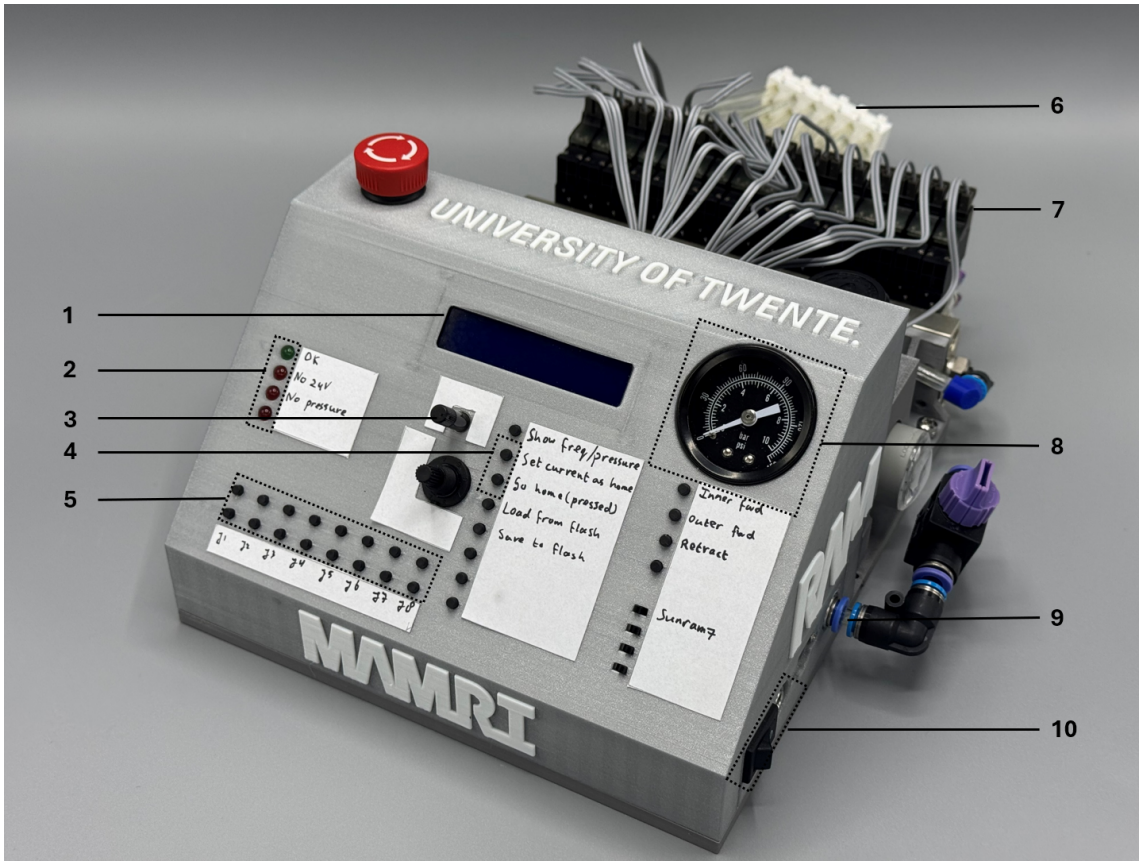

Figure 2.4: The controller used to actuate MAMRI, featuring: 1. Display to visualize the current number of steps taken for each motor, 2. Indicator light showing the status of the controller, 3. Potentiometer to control the step frequency, 4. Buttons to set the current position as home and to move to the home position, 5. Button for manual control of each motor position, 6. Air tube connector, 7. Pneumatic valves, 8. Barometer to control pressure, 9. Pressurized air supply, 10. 24V inlet and power switch.

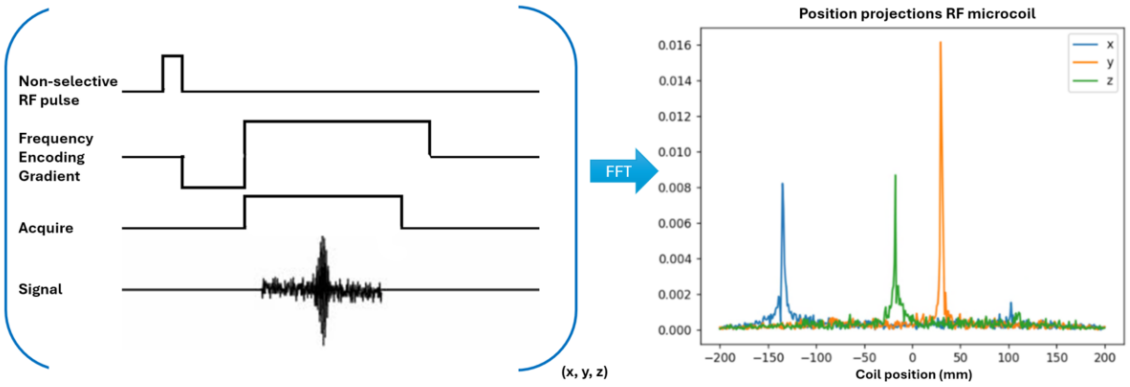

Figure 2.6: Schematic representation of the active tracking sequence and data acquisition process. A non-selective RF pulse is applied, followed by a frequency encoding gradient along each spatial axis. The acquired signals undergo a forward Fourier transform (FFT), resulting in distinct spectral peaks proportional to the location of the RF microcoil, which are provided by the scanner in the form of position projections.

single sharp peak can be observed in the frequency spectrum for a small volume sample placed within a receiver coil (RF microcoil) (Figure 2.5). This frequency is directly proportional to the location of the RF microcoil. The in-house developed RF microcoils are tuned to have an optimal reception sensitivity at 64.7 Hz.

A basic active tracking sequence involves a non-selective RF pulse, which excites all spins within the field of view (FoV). A frequency-encoded echo is then generated by applying a readout gradient pulse along one axis. The coils location along this axis is determined by performing a Fourier transformation on the acquired data (Figure 2.6). This process is repeatedly performed in the x, y and z readout direction, enabling precise localization of the RF microcoil in 3D space. Nowadays, sequences are used based on spoiled gradient echo (FLASH) and balanced steady state free procession (bSSFP) to improve the accuracy and tracking rates up to 50 fps with sub-millimetre accuracy [24], [25].

3 Methods

In this chapter, the methods used to design, develop, control and evaluate the performance of MAMRI concerning the research question as defined in 1.

3.1 Design and development

To adapt MAMRI for abdominal biopsy procedures, a biopsy needle-compatible end-effector must be integrated into the system. Two distinct workflows have been defined:

Manual Needle Injection: MAMRI positions a needle guide along the defined injection path. Software guidance would then be provided to assist a clinician in manually inserting the needle to a specific depth to reach the target.

Motorized Needle Placement: The end-effector is motorized to enable precise and rightly timed needle placement for a dynamic target. To address safety and ethical considerations, the clinician would be embedded in the safety protocol and retain control of the intervention.

To cover both workflows two distinct end-effectors were developed.

Additionally, a baseplate was designed to accurately fixate MAMRI to the table of a Siemens MRI system (Aera, Siemens, Erlangen, Germany) in the centre axis of the bore.

3.1.1 End-effector

To be able to easily switch between the end-effector mounted onto MAMRI a dovetail attachment was developed, as can be seen in Figure 3.1

For the manual needle injection workflow a needle guide was developed, which slides in on the dovetail attachment and is locked in place by a locking pin (Figure 3.1). The diameter of the end-effector was designed to be 64 mm to match up the size of a median pneumatic motor such as motors 1,3 and 4. These components were 3D printed from Polylactide (PLA) with a FDM printer (X1-Carbon, Bambulabs, Shenzhen, China).

The Motorized needle workflow is addressed using a M-45B pneumatic motor developed by V. Groenhuis (Enschede, Netherlands), which is integrated into the needle guide design (Figure 3.2). This motor drives a rack where the biopsy needle can be attached on, enabling the possibility to actuate the needle remotely with steps of 0.6 mm. This end-effector was designed to actuate a 14G 200 mm long MR-compatible semi-automatic biopsy gun (Innotom, Bochum, Germany).

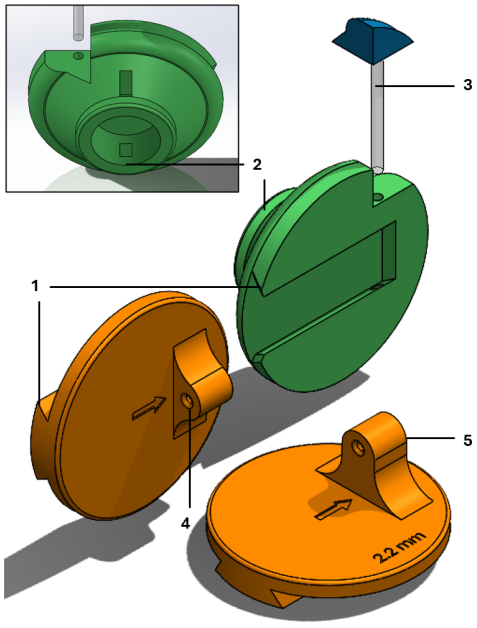

Figure 3.1: Design of the end-effector: 1. Dovetail connection for easy interchangeability of end-effectors, 2. Connection mount to connect with MAMRI, 3. Acrylic locking pin fixed into the pin holder, 4. Needle guide for a 15-gauge biopsy needle, 5. Needle guide for a 14-gauge biopsy needle.

3.1.2 Baseplate

To make the baseplate universally usable for positioning MAMRI in various locations for different applications, a 4 × 8 grid of M6 tapped holes with 50 mm spacing was designed (Figure 3.3). The base-

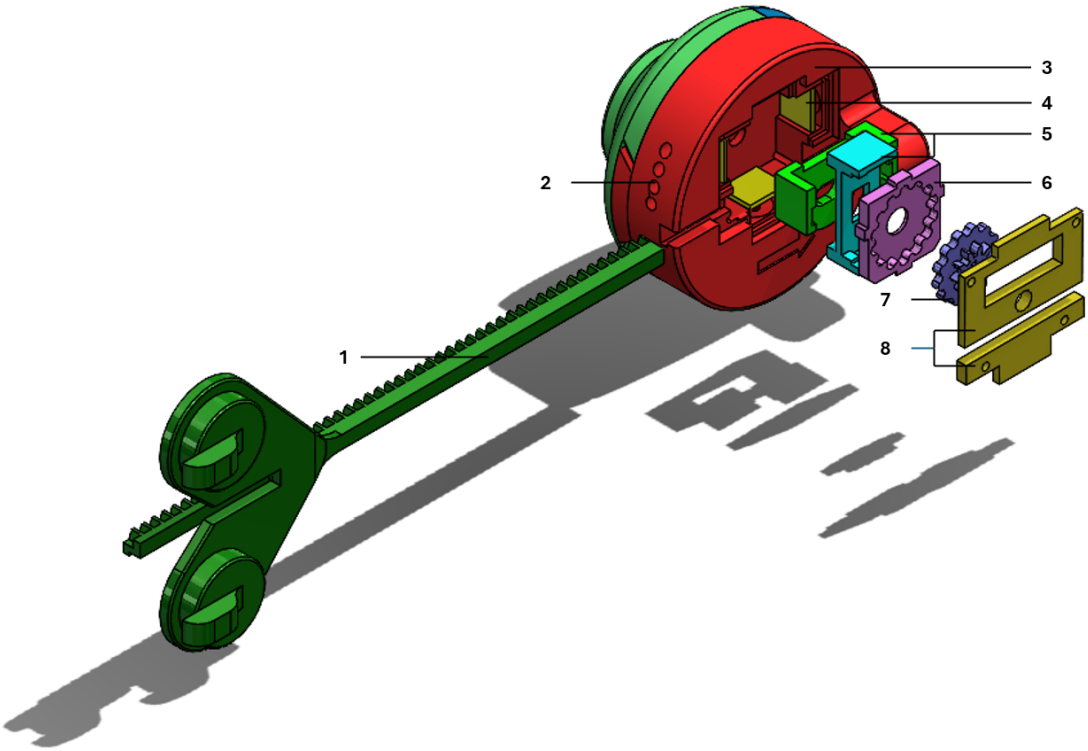

Figure 3.2: Exploded view of the motorized end-effector: 1. Needle driving rack, 2. pneumatic tubing inlets for driving the embedded M-45B motor, 3. Needle guide with embedded M-45B motor (V. Groenhuis, Enschede, Netherlands) housing, 4. Seals (4x), 5. Pistons (2x), 6. Hoop gear, 7. Cycloid gear with pinion, 8. Motor housing cover.

plate was laser-cut from 10 mm thick acrylate, and four click-in sliders were developed and 3D printed from PLA to precisely clamp the baseplate into the gutters of a conventional Siemens MR table. The design also features cut-outs along the sides to maintain compatibility with additional attachments, such as MRI coils or fixation belts. In this research, MAMRI was secured at the centre of the plate, marked by a small plus sign, using four nylon screws and 1 mm thick O-rings placed between the plate and MAMRI.

3.2 Kinematics

To actuate MAMRI, a 6-DoF robot, to a specific position, kinematics were considered. Forward kinematics were used to determine the position of the end-effector based on the joint angles. The inverse process described the joint angles when the (target) position of the end-effector was known.

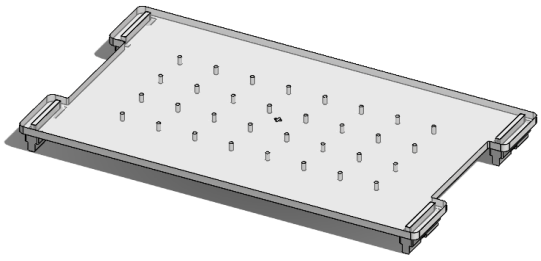

Figure 3.3: The developed universal baseplate for Siemens MR table fixation

For MAMRI, these calculations were approached analytically. By using the spherical nature of the end-effector, efficient and direct solutions for joint configurations could be derived. This approach is particularly advantageous for real-time implementations, where computational speed is important. Besides, a fully functionally analytical kinematics model could be easily adjusted for other tailored dimensions of MAMRI.

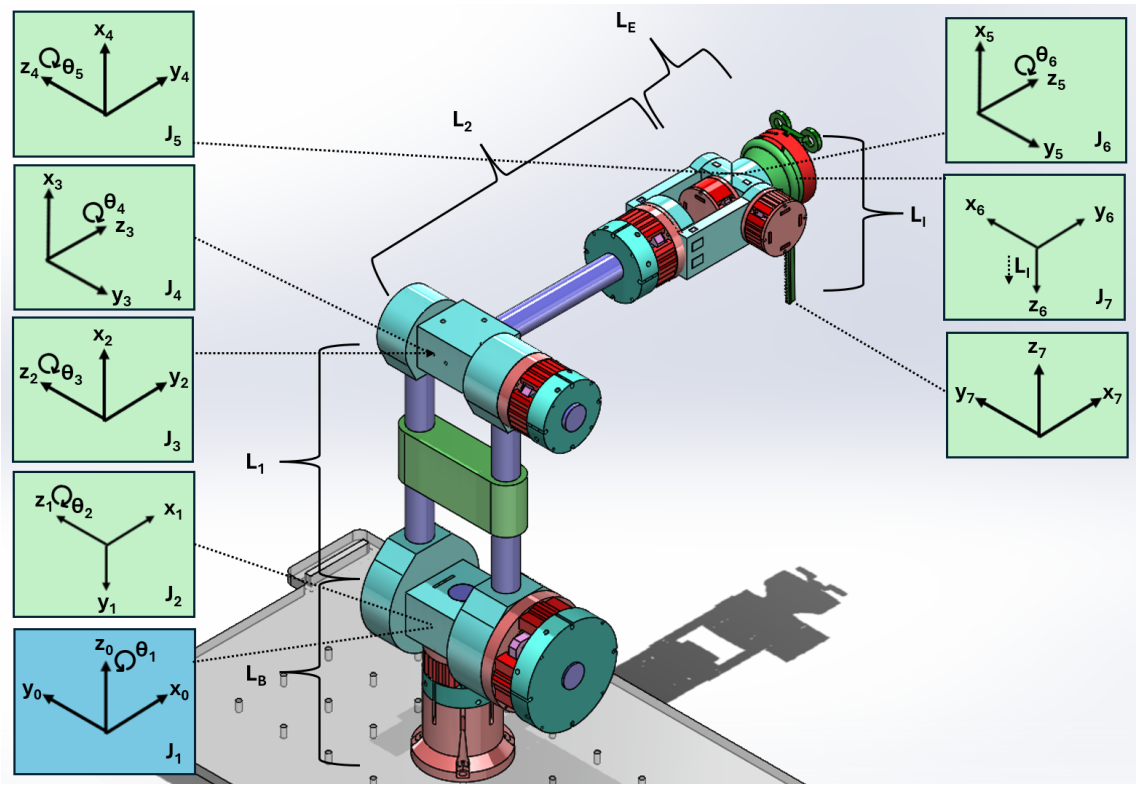

Figure 3.4: DH-Frame distribution of MAMRI including the motorized end-effector, as joint 7. The attachment position of each frame is indicated with a dotted-line, the base frame (f_0) is indicated in blue

For the analytical approach homogenous transformation matrices are utilized to define the rotation and translation from frame n to frame n+1, as indicated in equation 3.1. These frames are distributed by the Denavit Hartenberg (DH) convention as illustrated in Figure 3.4. Based on this frame distribution the DH parameters indicated in (table 3.1) were found. A frame was indicated as f_n with n being the joint number (J_n) minus 1, with f_0 being the base frame of MAMRI.

$$q_n = {}^{n-1}_{n}T \cdot q_{n-1} \tag{3.1}$$

With these DH parameters the homogenous transformation matrix ${}^{n-1}_{n}T$ was defined as;

Table 3.1: Denavit-Hartenberg parameters for the 6-DoF MAMRI robotic arm.

i	θ **(rad)**	α **(rad)**	**a (cm)**	**d (cm)**
1	θ_1	$-\frac{\pi}{2}$	0	L_B
2	$\theta_2 - \frac{\pi}{2}$	0	L_1	0
3	θ_3	$-\frac{\pi}{2}$	0	0
4	θ_4	$\frac{\pi}{2}$	0	L_2
5	θ_5	$-\frac{\pi}{2}$	0	0
6	$\theta_6 - \frac{\pi}{2}$	$\frac{\pi}{2}$	0	L_E
7	$\frac{\pi}{2}$	π	0	L_I

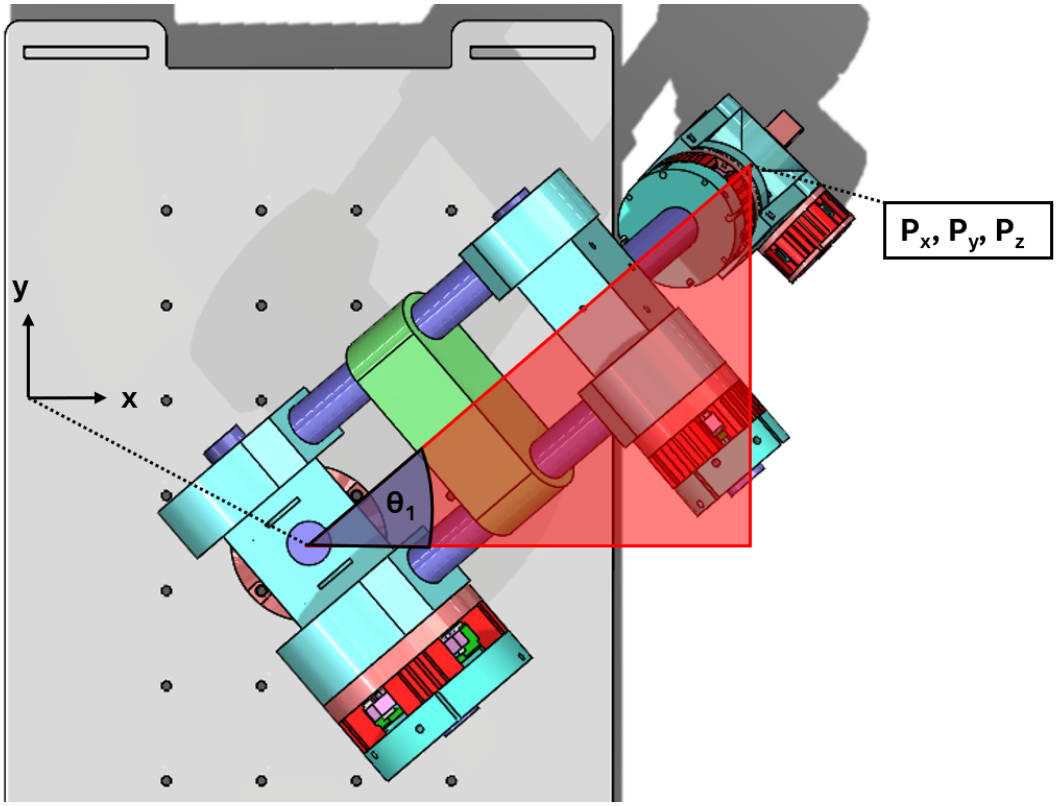

Figure 3.5: Top view of MAMRI to visualize the geometrical approach for the expression of θ_1.

$$ {}^{n-1}_{n}T = \begin{bmatrix} \cos(\theta)_n & -\sin(\theta)_n\cos(\alpha)_n & \sin(\theta)_n\sin(\alpha)_n & a_n\cos(\theta)_n \\ \sin(\theta)_n & \cos(\theta)_n\cos(\alpha)_n & -\cos(\theta)_n\sin(\alpha)_n & a_n\sin(\theta)_n \\ 0 & \sin(\alpha)_n & \cos(\alpha)_n & d_n \\ 0 & 0 & 0 & 1 \end{bmatrix} \tag{3.2} $$

The homogeneous transformation matrix was utilized to calculate the position of the needle tip, represented by coordinate frame 7, based on the joint positions at any given time (forward kinematics). This enabled the evaluation of the kinematic model by comparing the predicted needle tip position from the model with the measured needle position obtained by active tracking.

The the first three rows and columns of ${}^{n-1}_{n}T$ defined the rotation matrix ${}^{n-1}_{n}R$. Due to the spherical design of the end-effector wrist, the inverse kinematics problem could be decomposed into two sub-problems:

- The first three joint angles determine the position of the end-effector.
- The resulting joint angles determine the orientation of the end-effector.

The joint angles for the first three joints were determined by a geometrical approach. This approach is indicated in Figures 3.5 and 3.6, resulting in equations 3.3, 3.4, 3.5 and 3.6.

$$ \theta_1 = \arctan 2(\mathrm{P}_y, \mathrm{P}_x) \tag{3.3} $$

$$ r_1 = \sqrt{\mathrm{P}_x^2 + \mathrm{P}_y^2 + (\mathrm{P}_z - L_B)^2} \tag{3.4} $$

$$ \theta_2 = \frac{\pi}{2} - \arctan 2\left(\mathrm{P}_z - L_B, \sqrt{\mathrm{P}_x^2 + \mathrm{P}_y^2}\right) - \arccos\left(\frac{L_1^2 + r_1^2 - L_2^2}{2L_1 r_1}\right) \tag{3.5} $$

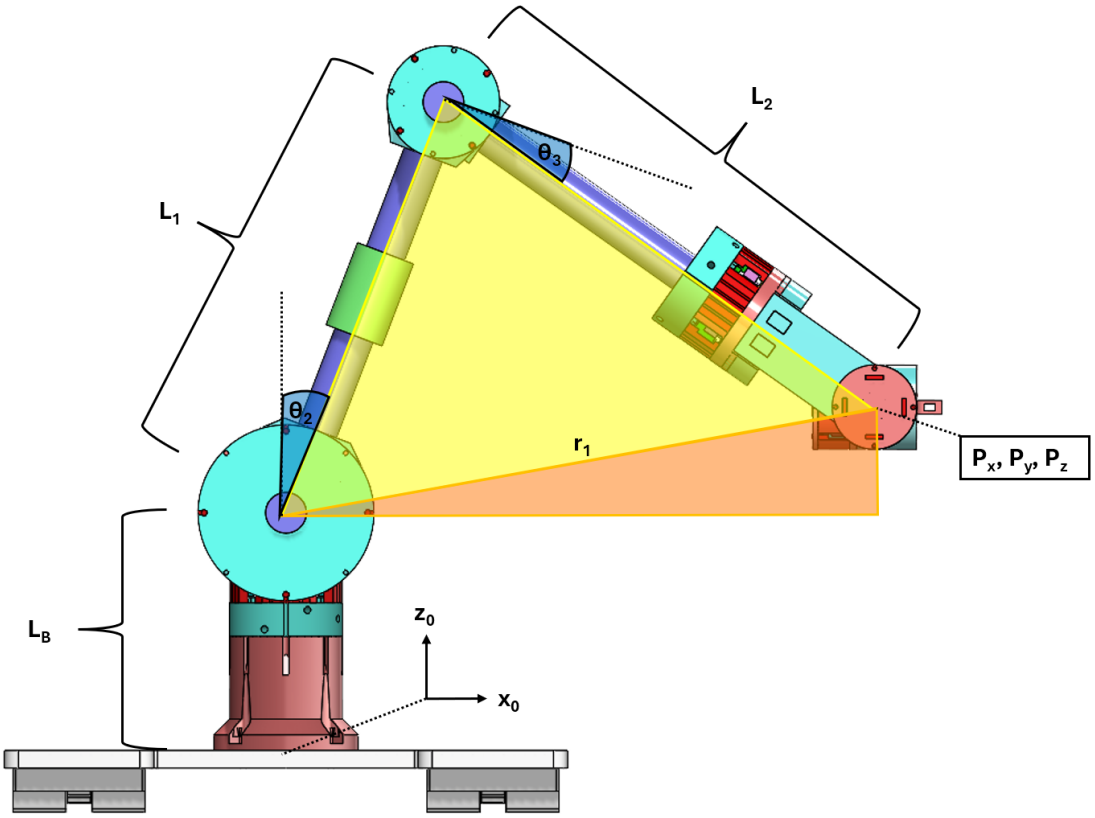

Figure 3.6: Side view of MAMRI to visualize the geometrical approach for the expressions of θ_2 and θ_3.

$$\theta_3 = \frac{\pi}{2} - \arccos\left(\frac{L_1^2 + L_2^2 - r_1^2}{2L_1L_2}\right) \tag{3.6}$$

With the values of θ_1,θ_2,θ_3 and the DH parameters the rotation matrix ${}^0_3R$ was determined using 3.2 formula 3.7.

$${}^0_3R = {}^0_1R \cdot {}^1_2R \cdot {}^2_3R \tag{3.7}$$

By using the inverse of this matrix the rotation matrix (${}^3_{7_d}R$) from joint 3 to the end-effector frame (f_7) was calculated. However, since ${}^0_3R$ is a square orthogonal rotation matrix and has a non-zero determinant, the transpose of the matrix is equal to the inverse. Calculating the transpose is less computationally demanding and faster, which is an advantage in real-time implementations.

$${}^3_{7_d}R = \left({}^0_3R\right)^{-1} \cdot {}^0_{7_d}R \tag{3.8}$$

The matrix $R^0_{7_d}$ is defined by the input parameters, stating the rotation of the end-effector frame (f_7) relative to the base frame (f_0) around the x_{f_0}, y_{f_0} and z_{f_0}-axis.

$${}^0_{7_d}R = \begin{bmatrix} 1 & 0 & 0 \\ 0 & \cos(\theta_x) & -\sin(\theta_x) \\ 0 & \sin(\theta_x) & \cos(\theta_x) \end{bmatrix} \cdot \begin{bmatrix} \cos(\theta_y) & 0 & \sin(\theta_y) \\ 0 & 1 & 0 \\ -\sin(\theta_y) & 0 & \cos(\theta_y) \end{bmatrix} \cdot \begin{bmatrix} \cos(\theta_z) & -\sin(\theta_z) & 0 \\ \sin(\theta_z) & \cos(\theta_z) & 0 \\ 0 & 0 & 1 \end{bmatrix} \tag{3.9}$$

By the use of the Homogeneous transformation matrixes derived by the DH-Parameters (3.2) the rotation matrix ${}^3_7R$ was calculated symbolically, equation 3.10 and matrix 3.11.

$$ {}^{3}_{7}R = {}^{3}_{4}R \cdot {}^{4}_{5}R \cdot {}^{5}_{6}R \cdot {}^{6}_{7}R \tag{3.10} $$

$$ {}^{3}_{7}R = \begin{bmatrix} -\sin(\theta_5)\cos(\theta_4) & -\sin(\theta_4)\sin(\theta_6-\frac{\pi}{2}) + \cos(\theta_4)\cos(\theta_5)\cos(\theta_6-\frac{\pi}{2}) & -\sin(\theta_4)\cos(\theta_6-\frac{\pi}{2}) - \sin(\theta_6-\frac{\pi}{2})\cos(\theta_4)\cos(\theta_5) \\ -\sin(\theta_4)\sin(\theta_5) & \sin(\theta_4)\cos(\theta_5)\cos(\theta_6-\frac{\pi}{2}) + \sin(\theta_6-\frac{\pi}{2})\cos(\theta_4) & -\sin(\theta_4)\sin(\theta_6-\frac{\pi}{2})\cos(\theta_5) + \cos(\theta_4)\cos(\theta_6-\frac{\pi}{2}) \\ \cos(\theta_5) & \sin(\theta_5)\cos(\theta_6-\frac{\pi}{2}) & -\sin(\theta_5)\sin(\theta_6-\frac{\pi}{2}) \end{bmatrix} \tag{3.11} $$

By knowing the structure of the terms of the matrix elements of ${}^{3}_{7_d}R$ from ${}^{3}_{7}R$ the joint angles θ_4,θ_5,θ_6 where calculated by the following formula's.

$$ \theta_5 = -\arccos\left(\left[{}^{3}_{7_d}R\right]_{3,1}\right), \quad \text{where } \theta_5 \in [-\pi, \pi] \tag{3.12} $$

$$ \theta_4 = \arctan 2\left(\frac{\left[{}^{3}_{7_d}R\right]_{2,1}}{-\sin(\theta_5)}, \frac{\left[{}^{3}_{7_d}R\right]_{1,1}}{-\sin(\theta_5)}\right), \quad \text{where } \theta_4 \in [-\pi, \pi] \tag{3.13} $$

$$ \theta_6 = \arctan 2\left(\frac{\left[{}^{3}_{7_d}R\right]_{3,3}}{-\sin(\theta_5)}, \frac{\left[{}^{3}_{7_d}R\right]_{3,2}}{\sin(\theta_5)}\right) + \frac{\pi}{2}, \quad \text{where } \theta_6 \in [-\pi, \pi] \tag{3.14} $$

The validity of the derived transformation matrix, based on the obtained angles, was verified by comparing ${}^{3}_{7_d}R$ with ${}^{3}_{7}R$, ensuring that the calculated angles resulted in the desired end-effector orientation. The two rotation matrices had to be equal for the computed angles to be considered valid. To rule out invalid setpoints, only the obtained angles satisfying this condition were passed as valid setpoints. Redundancy is limited by forcing an elbow-up configuration, where the arm is always forward, and by setting appropriate joint angle limits.

3.3 RF microcoil localization

A vendor supplied active tracking sequence (BEAT, Siemens Healthineers, Erlangen, Germany) was utilized to acquire location projections with custom made RF microcoils (Figure 2.5) on a 1.5T MRI system (Magnetom Aera, Siemens Healthineers, Erlangen, Germany), located at the TechMed Centre, University of Twente, Enschede, Netherlands. Acquired data were transmitted to a remote PC using a vendor-supplied software interface (Access-i, Siemens Healthineers, Erlangen, Germany). This software interface enables bidirectional communication with the MR scanner, allowing remote control of acquisition protocol settings and facilitating data processing on a separate workstation. This enabled the integration with the robot controller. The software architecture for processing the data in this project was developed using the Python Access-i library created by M. Reinok as a basis.

The protocol settings of the active tracking sequence are shown in table 3.2. These settings resulted in a data output of 21.53 fps.

The dataset received through Access-i consisted of the x,y, and z location projections for each connected coil, as shown in Figure 2.6, The dataset was updated every 46.44 milliseconds (21.53 fps) with new location projections. Each spectrum had a length corresponding to the number of samples per projection, defined by the base resolution.

The physical distance between two consecutive sample points in space (Δx) was determined by dividing the Field of View (FoV) by the base resolution, which corresponds to the number of samples per projection, as defined in Equation 3.15:

$$ \Delta x = \frac{\text{FoV}}{\text{Base resolution}} = 0.78 \text{ mm} \tag{3.15} $$

Table 3.2: Scan parameters used in the scan template based on the tracking sequence

Property	Value
FOV	500 mm
TR	7.74 ms
TE	5.10 ms
Averages	2
Base Resolution	640
Bandwidth	300 Hz/Px
Background Suppression	1 mT/m
Flip Angle	20°

Table 3.3: Stepping frequencies for the pneumatic motors of MAMRI

Joint	frequency (Hz)	Angular speed ($^\circ/s$)
1	15	3.15
2	12	1.68
3	15	3.30
4	15	3.15
5	20	5.60
6	20	5.60

By multiplying the index of the highest observed peak location in the projection spectrum by the spatial resolution (Δx) and subtracting half the Field of View (FoV) to account for the MRI isocenter, the position of the RF microcoil (p_i) along the x,y and z axes could be determined with a precision of Δx.

$$p_i = (i_{\max} \cdot \Delta x) - \frac{\text{FoV}}{2} \pm \Delta x, \quad i_{\max} \in x, y, z \tag{3.16}$$

3.4 Control

This section discusses the main components involved in controlling and actuating MAMRI, including the developed graphical user interface (GUI), calibration and collision avoidance protocols. To actuate MAMRI the controller described in Section 2.2 was used. The pneumatic valves were operated a 3 bar. Five-meter pneumatic tubing was used to connect the pneumatic motors of MAMRI, positioned inside the MRI, to the controller, which was placed in the control room. Each motor was actuated at its optimal speed (Table 3.3) based on the specific combination of pressure and tubing length. The control system for MAMRI was implemented in Python.

3.4.1 Graphical User Interface

A Graphical User Interface (GUI) (Figure 3.8) was developed to facilitate the intuitive and user-friendly actuation of MAMRI. The GUI enables users to initiate standard protocols, such as calibration and the calculation of kinematic configurations required to reach a manually set setpoint. When the GUI is initiated, a choice must be made between a lab experiment, leading to a less constrained collision avoidance protocol, or an MRI experiment. The MRI experiment button also initiates the connection with the MR-scanner via Access-I and the tracking sequence. For both experiment types, the main functionalities are identical, including 'Emergency STOP', 'Move to base configuration', manually inputting a setpoint and 'Move MAMRI to setpoint'. However, after calibration to MRI space, as described in Section 3.4.2, all the functionalities of the GUI are enabled, as shown in Figure 3.8.

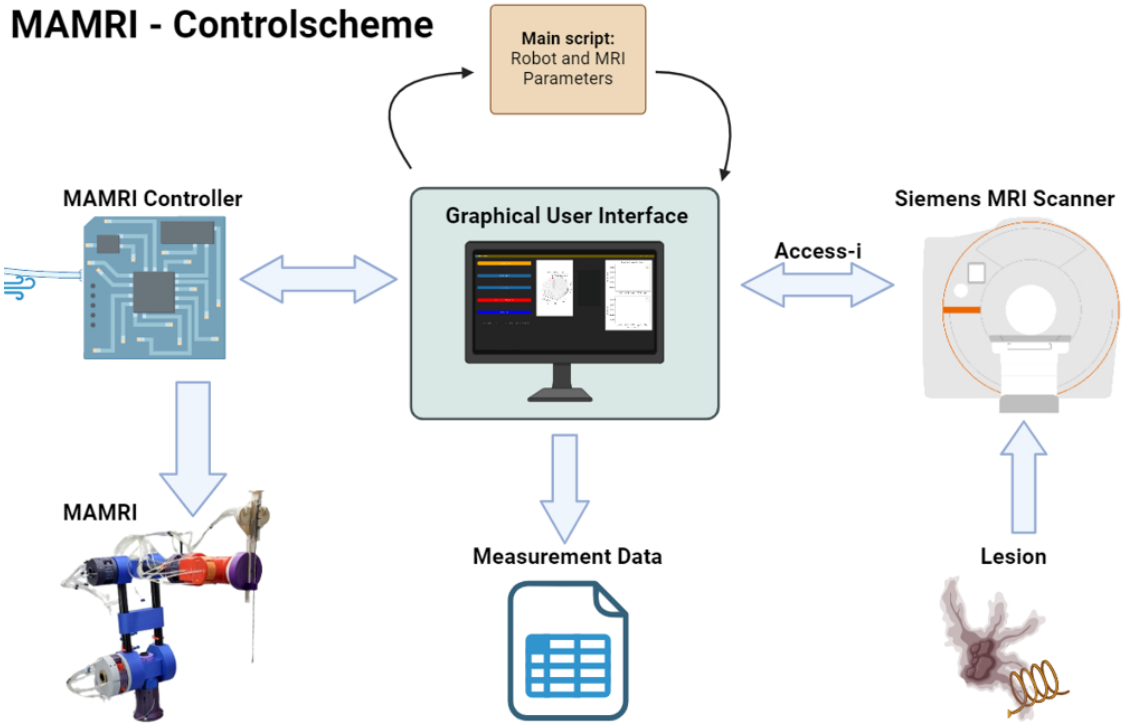

Figure 3.7: Schematic overview of the control scheme used within this research

3.4.2 Calibration

To actuate MAMRI towards a target identified by the MR scanner, a calibration process was implemented to determine the location of MAMRI within the MRI frame (f_m). An RF microcoil was attached to a 3D-printed coil holder (Figure 3.10), which was secured in the pneumatically motorized end-effector at a length of 110 mm distal from the rotation axis of joint 6 (Figure 3.2. The location of the solenoid of this RF microcoil was defined as surrogate needle tip.

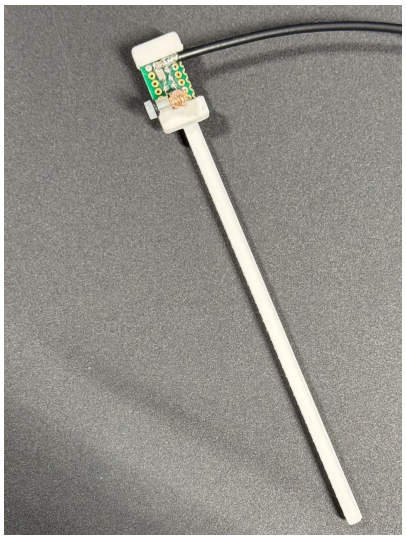

Figure 3.10: 3D-printed coil holder to attach the RF microcoil to MAMRI as surrogate needle

The calibration process started by running the tracking sequence via the graphical user interface (Section 3.4.1 and Figure 3.7). Before starting the calibration, it was confirmed that the robot was positioned in the L-shaped base configuration and placed within the bore of the scanner. The calibration button was then used to initiate the automated calibration process for MAMRI.

During calibration, the position of the RF microcoil on the needle was determined using the tracking sequence and expressed in the MRI frame (f_m) in millimetres indicated in Figure 3.9. This position was subsequently transformed into the robot's base frame orientation, being in centimetres. Using this position recording, together with the robot parameters and the initial joint angles in the L-shaped base configuration, the location of the base frame (f_0) was calculated relative to the MR scanner. This base location was saved and used thereafter to convert recorded coil positions to the base frame of the MAMRI.

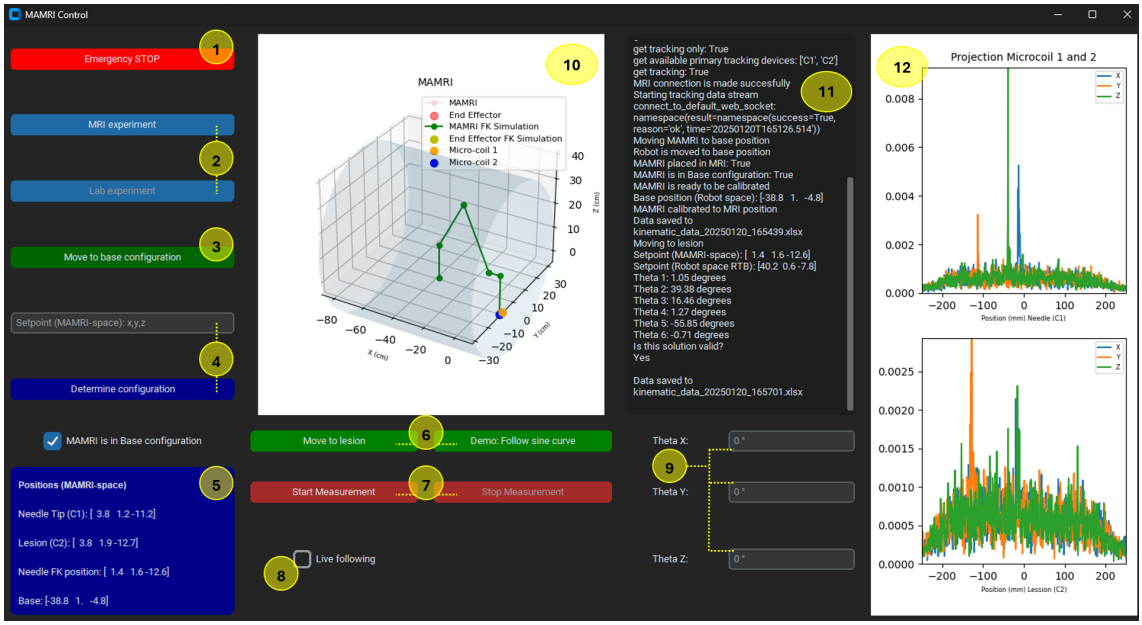

Figure 3.8: Overview of the developed graphical user interface, with key functionalities indicated: 1. Emergency stop to freeze MAMRI in its current position, 2. Buttons to switch between a lab experiment and an MRI experiment, determining the applicable collision avoidance protocols and functionalities, 3. Button to move MAMRI to its base position, 4. Textbox for manually inputting a setpoint and a button to compute the required kinematic configuration to reach it, 5. Real-time positions (21.53 fps) for the two microcoils, the base, and the predicted needle position based on forward kinematics, 6. Buttons to initiate MAMRI movement towards microcoil 2 or to track a virtual target following a sinusoidal trajectory along the x_m-direction, 7. Buttons to start, stop, and save the recorded positions of the microcoils and forward kinematic predictions to a .xlsx file, 8. Checkbox to enable continuous tracking of microcoil 2 by MAMRI, 9. Textboxes to adjust the orientation of the end-effector relative to the base needle-down orientation, 10. Live schematic visualization of MAMRI's computed and set orientation, including coil locations, 11. Logging display showing system responses to user input, 12. Real-time (21.53 fps) projection spectra for both coils.

.

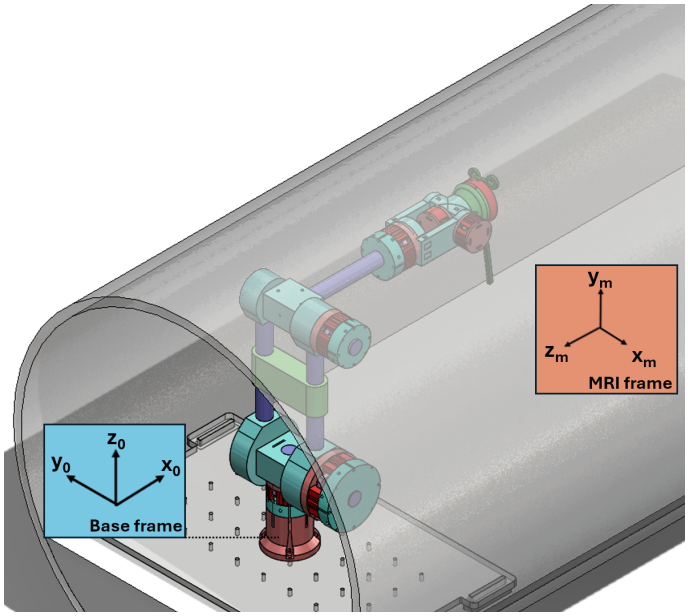

Figure 3.9: Visualisation of the MRI frame (f_m) orientation relative to the base frame (f_0) of MAMRI.

Table 3.4: Joint limits for collision avoidance of arm segments

Joint	limitation (°)
2	$-90 \leq q_2 \leq 90$
3	$-60 \leq q_3 \leq 60$
5	$-120 \leq q_5 \leq 120$

3.4.3 Collision avoidance

To prevent collisions between the end-effector and the bore, a collision avoidance protocol was implemented, consisting of a spherical safety margin depending on the chosen needle length (L_N) and end-effector. This margin was centred around the intersection of the joint axes (J5-J6) and determined by Equation 3.17.

$$r_s = \sqrt{L_N^2 + L_E^2} \tag{3.17}$$

Additionally, collisions between the needle tip and the table were avoided by restricting the minimum y_m position of the needle to 10 mm below the base frame (f_0) of MAMRI. Collisions of MAMRI with itself were also avoided by setting limits to angles of joints 2,3, and 5, as depicted in Table 3.4. Only setpoints where the safety margin did not intersect with the bore or table and were within the angle limitations were considered safe and were passed for actuation.

3.5 RF microcoil tracking

To assess the quality and consistency of the RF microcoil position measurements, a repeatability test was conducted by acquiring tracking data for a period of 160 seconds test with the RF microcoils stationary positioned inside the bore.

To evaluate the consistency of tracking data across multiple angles and axial orientations, the microcoil mounted at the distal end of the end-effector was used as surrogate needle (Figure 3.10). The tip of the surrogate needle was positioned near the central axis of the bore, corresponding to the point $(40, 0, 15)_{f_0}$ relative to the MAMRI base frame (f_0). Joint 6 was actuated in the positive direction with an angular speed of 2.8 $^\circ/s$ (10 Hz step frequency) to produce a circular motion of the coil around the z_{f_m}-axis with a radius of 105 mm. During this motion, the RF microcoil position was measured over time. For these measurements, a different scan protocol was used, based on the protocol as described in Table 3.2, but with FoV of 400 mm, a frame rate of 43.06 fps, and a spatial resolution of Δx = 1.0 mm. This measurement process was repeated for circular movements around the y_{f_m} and x_{f_m}-axes of the MRI to evaluate the consistency of tracking data for all RF microcoil orientations.

3.6 MAMRI performance

The performance of MAMRI was evaluated by quantifying positioning accuracy using the Euclidean position error. This error was defined as the Euclidean distance, representing the geometrical length of the shortest vector between two points in 3D space. The RF microcoil attached to the surrogate needle enabled real-time tracking of the needle tip relative to the setpoint. Additionally, the predicted needle position from the forward kinematics model was compared with this actual position measured using active tracking. A second RF microcoil was used as surrogate anatomy and functioned as target.

To evaluate the performance of the motorized end-effector, the surrogate needle was actuated towards $(42, 0, 15)_{f_0}$. From this initial position, Joint 7 (the motorized needle guide) was actuated at speeds ranging from 3.2 mm/s to 4.1 mm/s in alternating directions. The location of the needle tip was tracked over time.

3.6.1 Static performance test

To evaluate the static performance of the robot, it was actuated towards a virtual target $(42,3,8)_{f_0}$ starting from the base configuration. The position information of the surrogate needle was compared with the setpoint and the forward kinematic prediction of the path.

Subsequently, the robot was directed toward the surrogate anatomical RF microcoil with a safety offset of 55 mm along the z_{f_0} direction. This coil was placed on the MRI table within the workspace of the MAMRI. Again, the position information of the surrogate needle was compared with the setpoint, and the kinematic model now defined by the location of the anatomical surrogate RF microcoil. This measurement was repeated twice with the same virtual target and anatomical surrogate RF microcoil location. The distance between these two points was again expressed as Euclidean position error.

3.6.2 Dynamic performance test

To evaluate the dynamic performance of the MAMRI, it was first actuated towards a virtual target $(45,0,17.5)_{f_0}$, then a virtual sinusoidal path was initiated along the y_{f_0} direction with a frequency of 0.1 Hz and an amplitude of 30 mm, which corresponded to the median liver dome displacement at a slow breathing rate, the location of the surrogate needle was tracked throughout the motion and compared to the needle position predicted by forward kinematics. This measurement was repeated for sinusoidal paths at frequencies of 0.2 Hz and 0.33 Hz, corresponding to normal breathing and hyperventilation rates [31].

Secondly, the robot was actuated towards the anatomical surrogate, this coil was attached to a plastic shaft inside the bore. The shaft was actuated by a linear actuator driven by a DC motor (12V, Diydeg, China) resulting in a horizontal motion parallel to the z_{f_m}-axis at a safe distance from the magnetic field. No signal interference was observed when the DC motor was activated.

The target was moved at a frequency of 0.12 Hz by the linear actuator along the S/I-axes of the MRI frame (z_{f_m}), with an amplitude of 30 mm. The positions of the surrogate needle and the anatomical surrogate were tracked for minimal 140 seconds, including data from the initial movement. The needle path predicted by the kinematics was compared with the real needle location measured using the active tracking sequence. This experiment was repeated at frequencies of 0.15 Hz and 0.2 Hz.

4 Results

Within this chapter, the data obtained from active tracking using RF microcoils, as described in Sections 3.5, 3.6.1, and 3.6.2, is presented. All measurement data for the RF microcoil locations was directly recorded and displayed in the MRI coordinate frame (f_m) as indicated in Figure 3.9, ensuring that the data remains entirely independent of any calibration calculations involving MAMRI.

4.1 RF microcoil tracking

The measurement of the stationary RF microcoils (Figure 4.1 and 4.2) shows the position data for the two RF microcoils over time. For coil 1 there are considerable fluctuations in the z_{f_m}-position (±0.78 mm), for coil 2 these are seen in the y_{f_m}-direction.

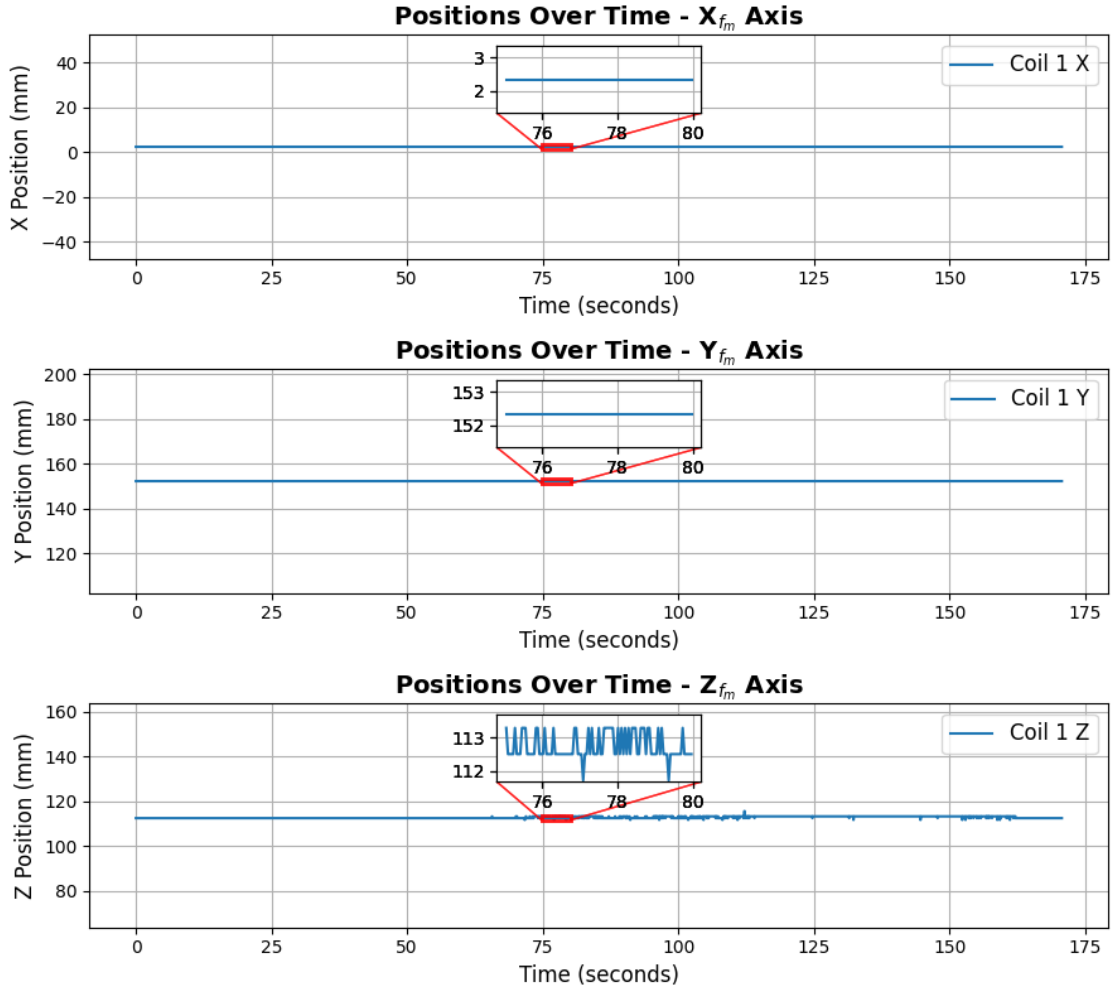

Figure 4.1: Position of RF microcoil 1 along each axis, including a 5-second zoom-in to assess data consistency. A stable signal is observed on the x_{f_m} and y_{f_m} axes, while the z_{f_m} axis shows considerable fluctuations between three sample point locations.

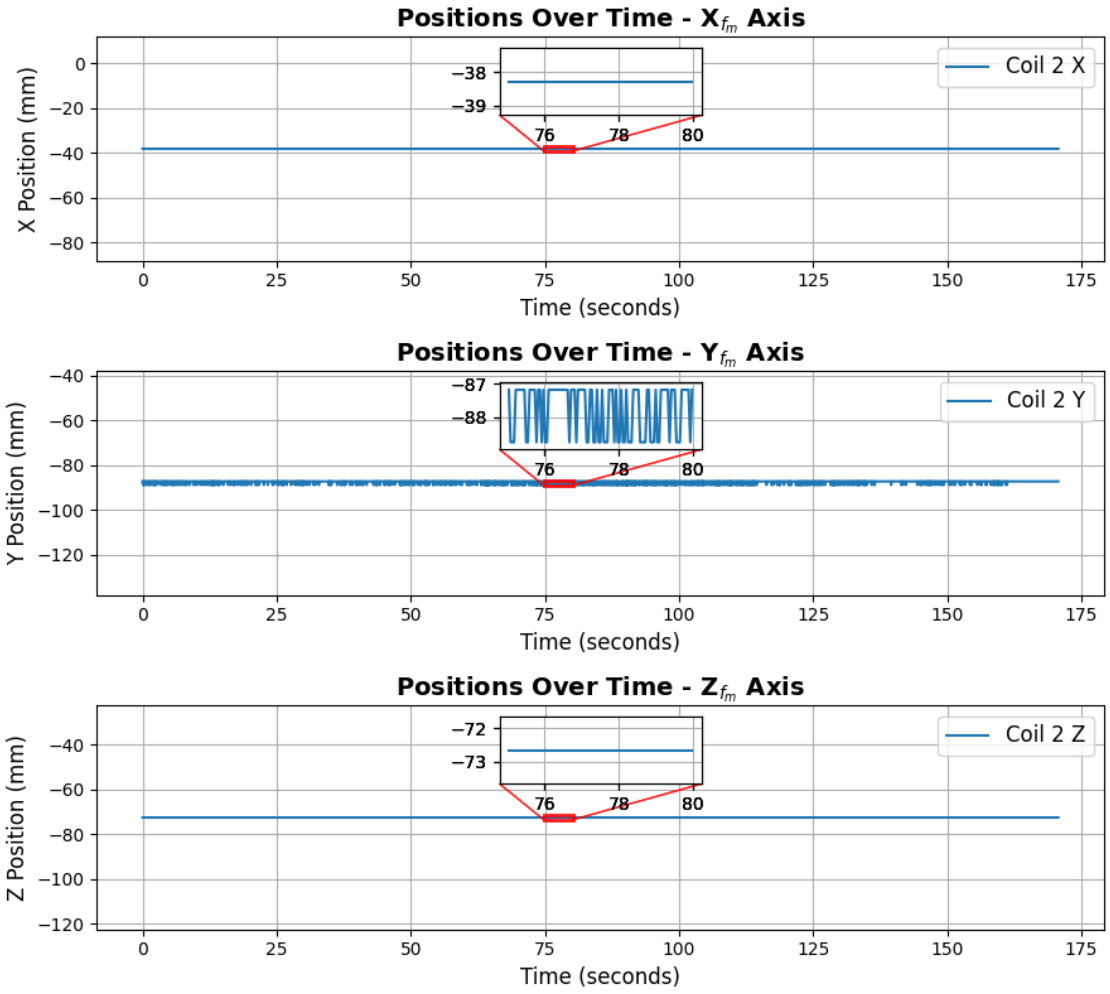

Figure 4.2: Position of RF microcoil 1 along each axis, including a 5-second zoom-in to evaluate data consistency. A stable signal is observed on the x_{f_m} and z_{f_m} axes, while the y_{f_m} axis shows considerable fluctuations between three sample point locations.

A circular path can be seen when an RF microcoil is rotated around the x_{f_m}-axis of the MRI frame (f_m) (Figures 4.3 and 4.4). High amounts of noise were observed when the solenoid was moved towards a position where it is parallel with B_0, which is orientated along the z_{f_m}-axis. This behaviour was also observed for a rotation around the y_{f_m}-axis (Figure 4.3,4.5). No concrete location could be determined when the RF microcoil was moved outside the Field of View. For the rotation around the z_{f_m}-axis (Figure 4.3 and 4.6) there is a high level of noise observed only when the solenoid direction is mirrored compared to the initial configuration.

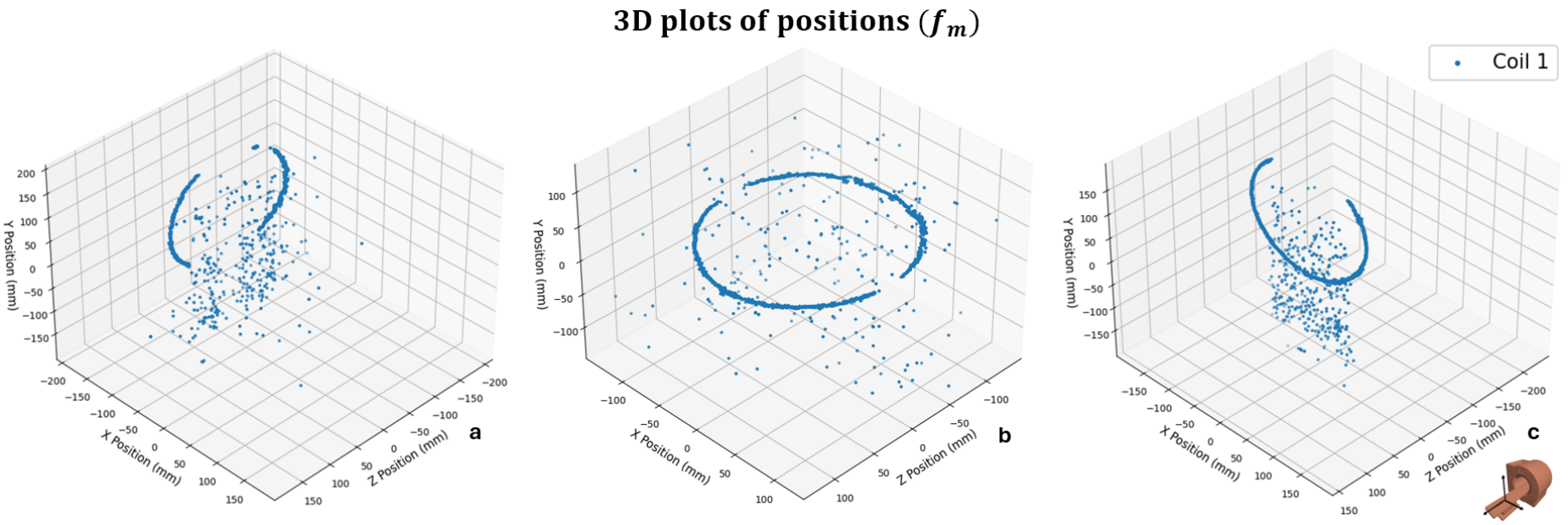

Figure 4.3: Position of the RF microcoil driven in a circular path around the (a). $\mathbf{x}_{f_m}$**-axis**, where a circular path is observed. However, for positions above $y_{f_m} = 200$, no constant location is detected. Additionally, when the solenoid was parallel to B_0, no concrete location was observed. (b). $\mathbf{y}_{f_m}$**-axis**, where a circular path is observed with location fluctuations when the solenoid was parallel to B_0 (c). $\mathbf{z}_{f_m}$**-axis**, where a circular path is observed, but no constant location was detected when the solenoid was mirrored compared to the initial configuration. The stepping frequency was 10 Hz.

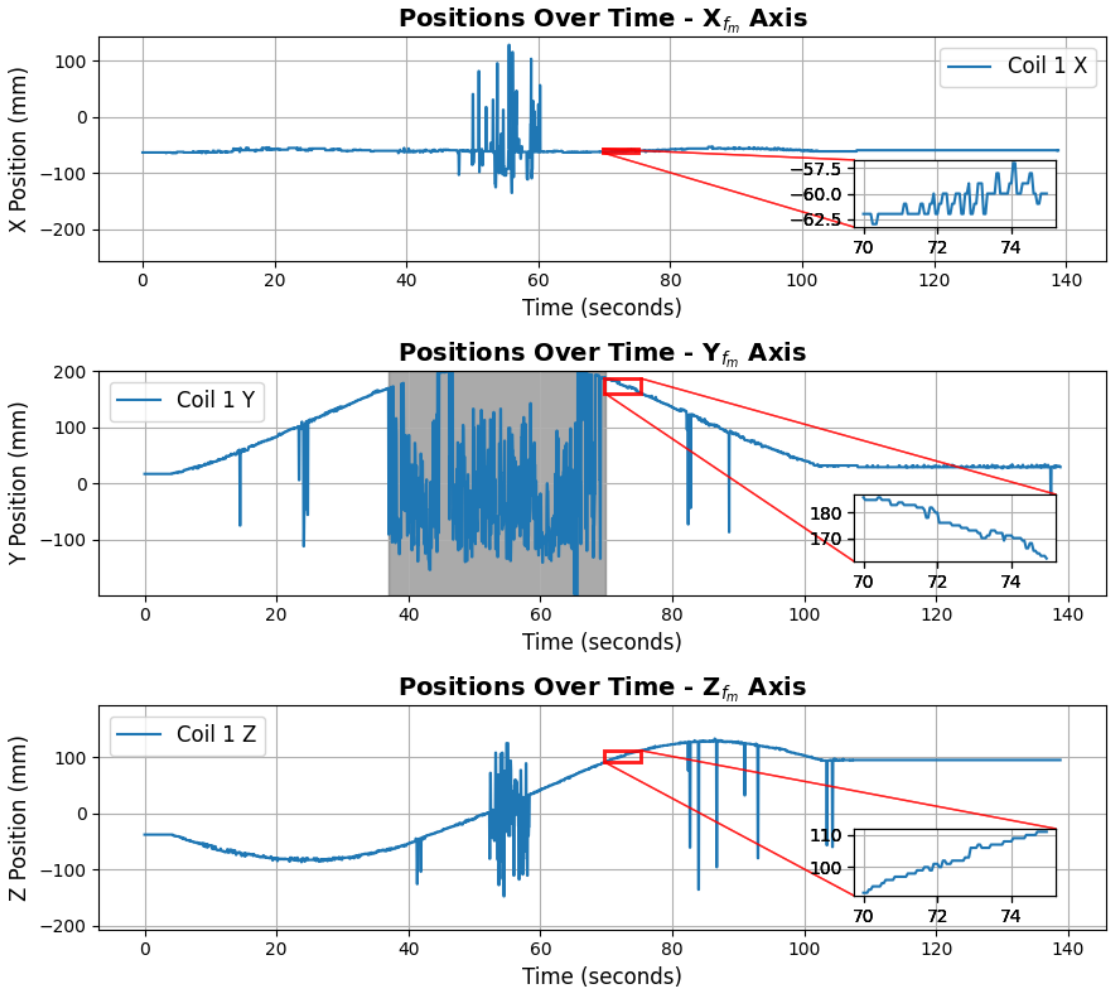

Figure 4.4: Position of the RF microcoil moving in a circular path around the x_{f_m}-axis with a stepping frequency of 10 Hz, shown for each axis, including a 5-second zoom-in to evaluate data consistency. The results indicate some fluctuations in the acquired position along the path. On the y_{f_m} and z_{f_m}-axes outliers are observed, appearing as vertical stripes, with some isolated occurrences, such as around t=85 seconds. The data within the grey area on the y_{f_m}-axis represents the noise observed when the coil was situated outside the Field of View (FoV) for the y_{f_m}-axes, for the other two axes there is considerable more noise observed when the solenoid was parallel orientated to B_0.

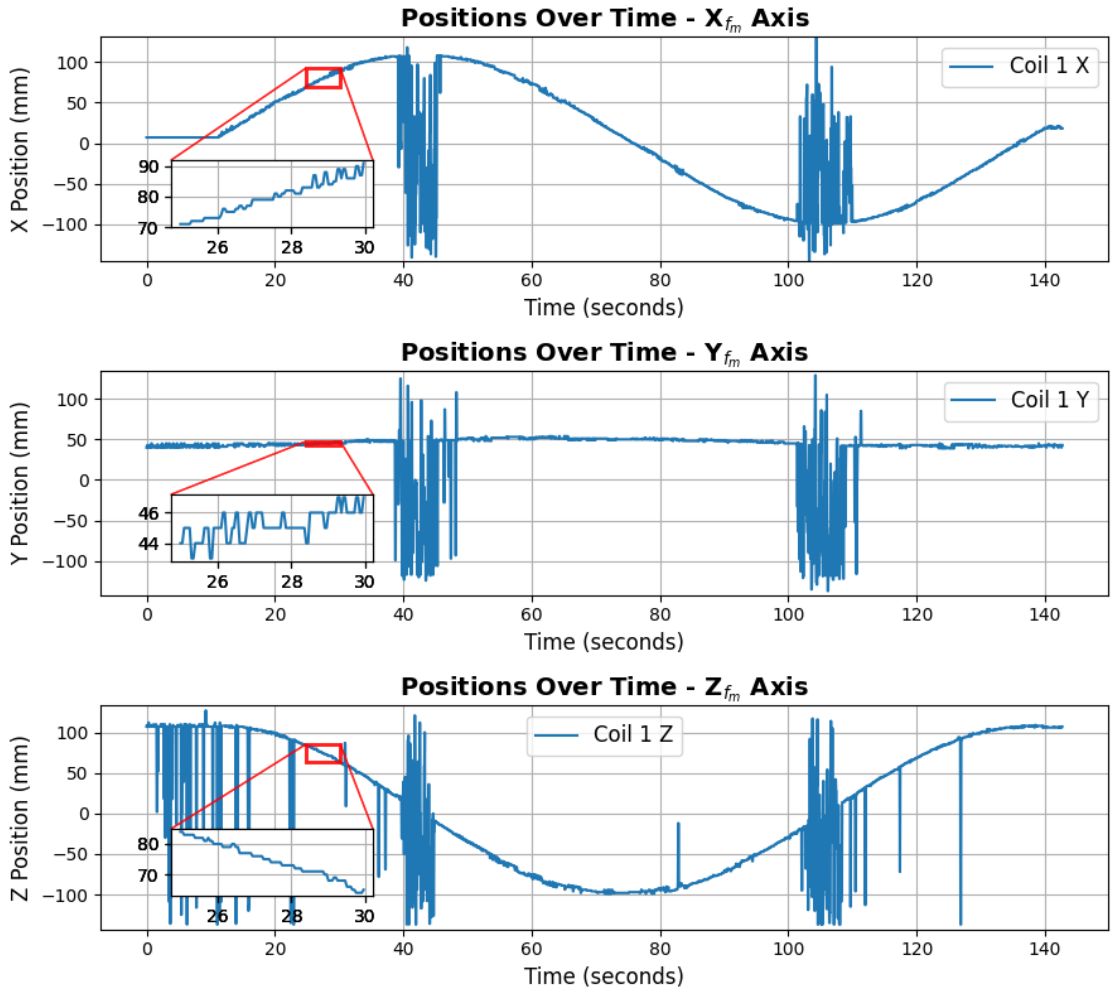

Figure 4.5: Position of the RF microcoil moving in a circular path around the y_{f_m}-axis with a stepping frequency of 10 Hz, shown for each axis, including a 5-second zoom-in to evaluate data consistency. The results indicate some fluctuations in the acquired position along the path. On the z_{f_m}-axis outliers are observed, appearing as vertical stripes, with some isolated occurrences, such as around t=5 seconds. There is considerably more noise observed when the solenoid was parallel orientated to B_0.

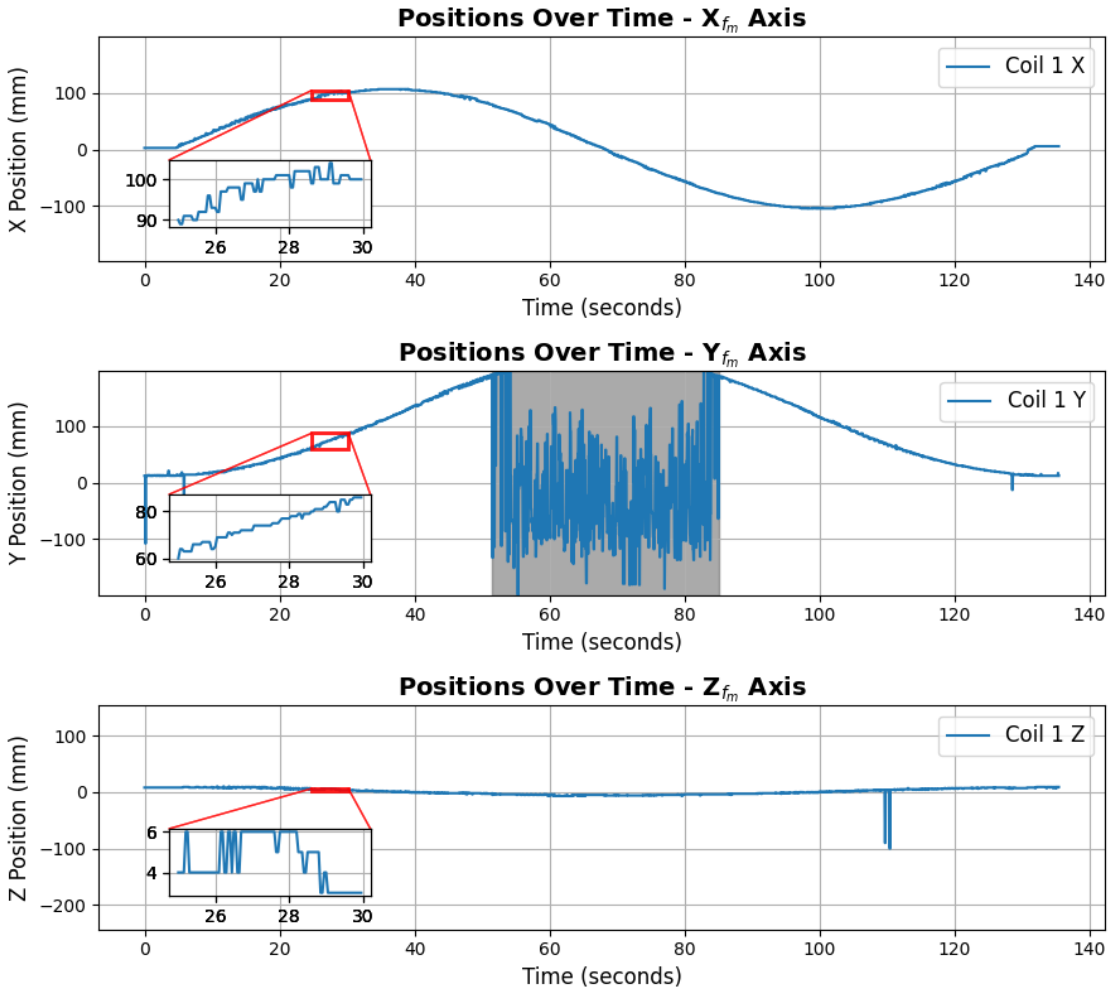

Figure 4.6: Position of the RF microcoil moving in a circular path around the z_{f_m}-axis with a stepping frequency of 10 Hz, shown for each axis, including a 5-second zoom-in to evaluate data consistency. The results indicate some fluctuations in the acquired position along the path. On the y_{f_m} and z_{f_m}-axes outliers are observed, appearing as vertical stripes, with some isolated occurrences, such as around t=110 seconds on the z_{f_m}-axis. The data within the grey area on the y_{f_m}-axis represents the noise observed when the coil was situated outside the Field of View (FoV) for the y_{f_m}-axes.

4.2 MAMRI performance

Figures 4.7 and 4.8 show a linear path of the surrogate needle tip in the y_{f_m}-direction of the MRI frame for four different speeds, with small oscillations in the x_{f_m} and z_{f_m} axis.

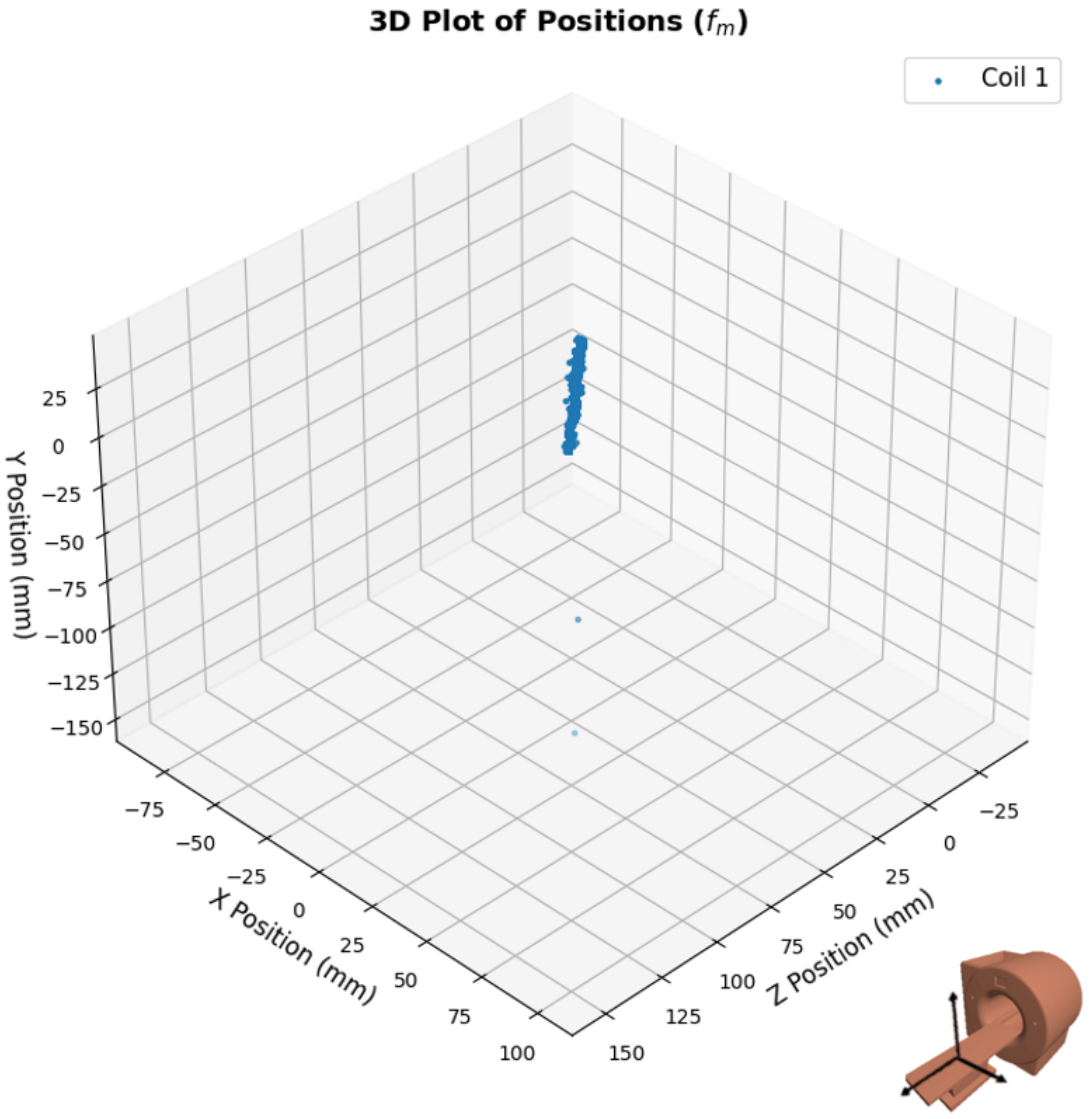

Figure 4.7: Position of the RF microcoil 1 (Surrogate Needle tip) moving in a linear path along the y_{f_m}-direction, actuated by the motorized needle guide. The trajectory appears slightly oblique in the x_{f_m} and z_{f_m}-directions.

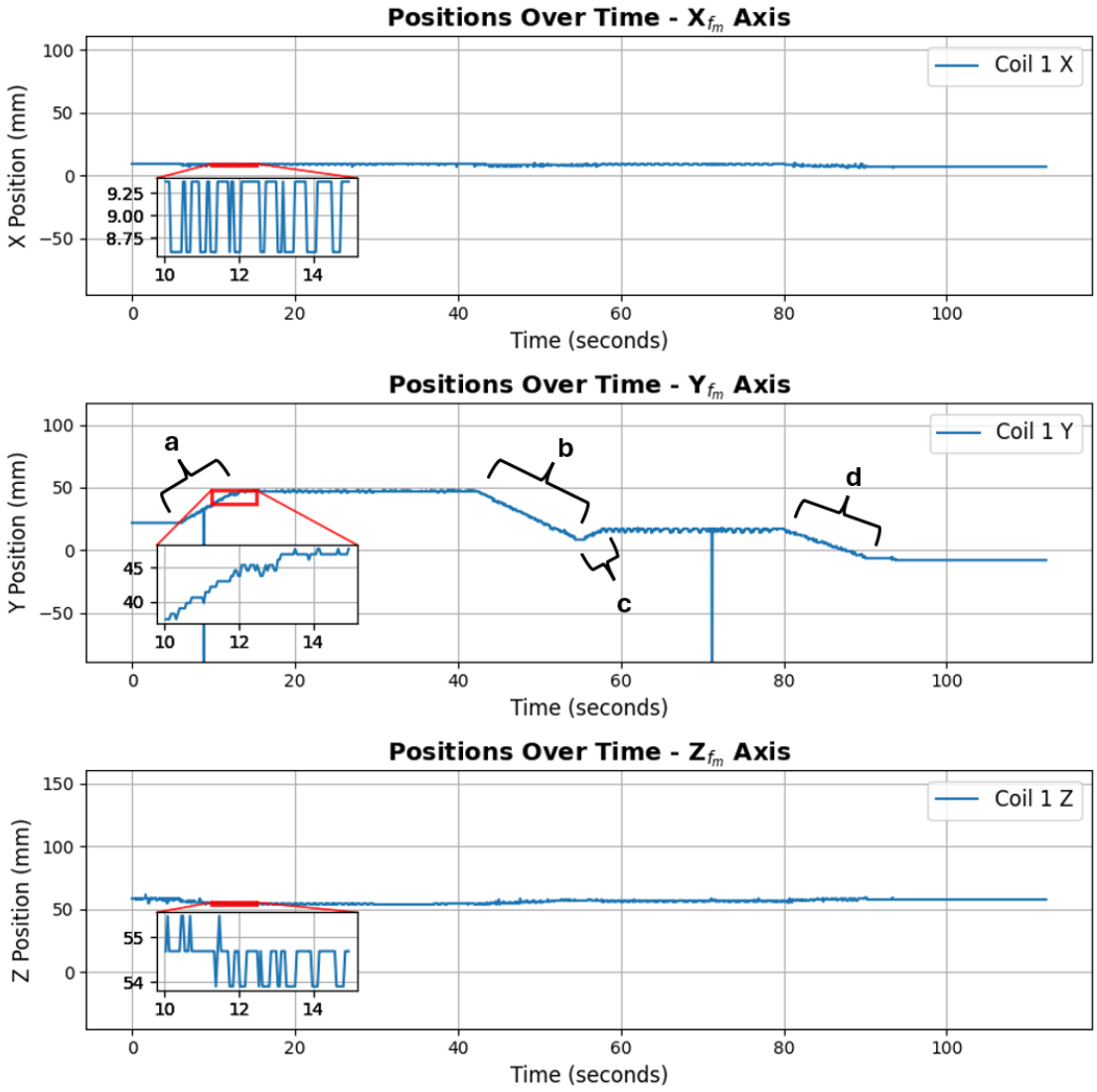

Figure 4.8: Position of the RF microcoil 1 (Surrogate Needle tip) moving in a linear path along the y_{f_m}-direction, actuated by the motorized needle guide, shown for each axis and including a 5-second zoom-in to evaluate data consistency. The results indicate some fluctuations in the acquired position along the path. On the y_{f_m} axis outliers are observed, appearing as vertical stripes, with some isolated occurrences, such as around t=77 seconds. Four needle injection speeds were observed: (a). 3.38 mm/s, (b). 3.23, (c). 4.14 mm/s, (d). 2.35 mm/s.

4.2.1 Static performance test

The data from the static performance test of MAMRI (Figures 4.9 and 4.10) shows the path of the needle tip, as measured by the RF microcoil, in comparison to the virtual target and the stationary target position defined by RF microcoil 2 and the predicted path by the forward kinematics. The location of coil 2 follows the position of the forward kinematic prediction with a small divergence on the axes. Table 4.1 shows the Euclidean error between the measured needle location and the setpoint. The Euclidean error between Coil 1 and Coil 2 approaches zero when MAMRI is actuated towards Coil 2.

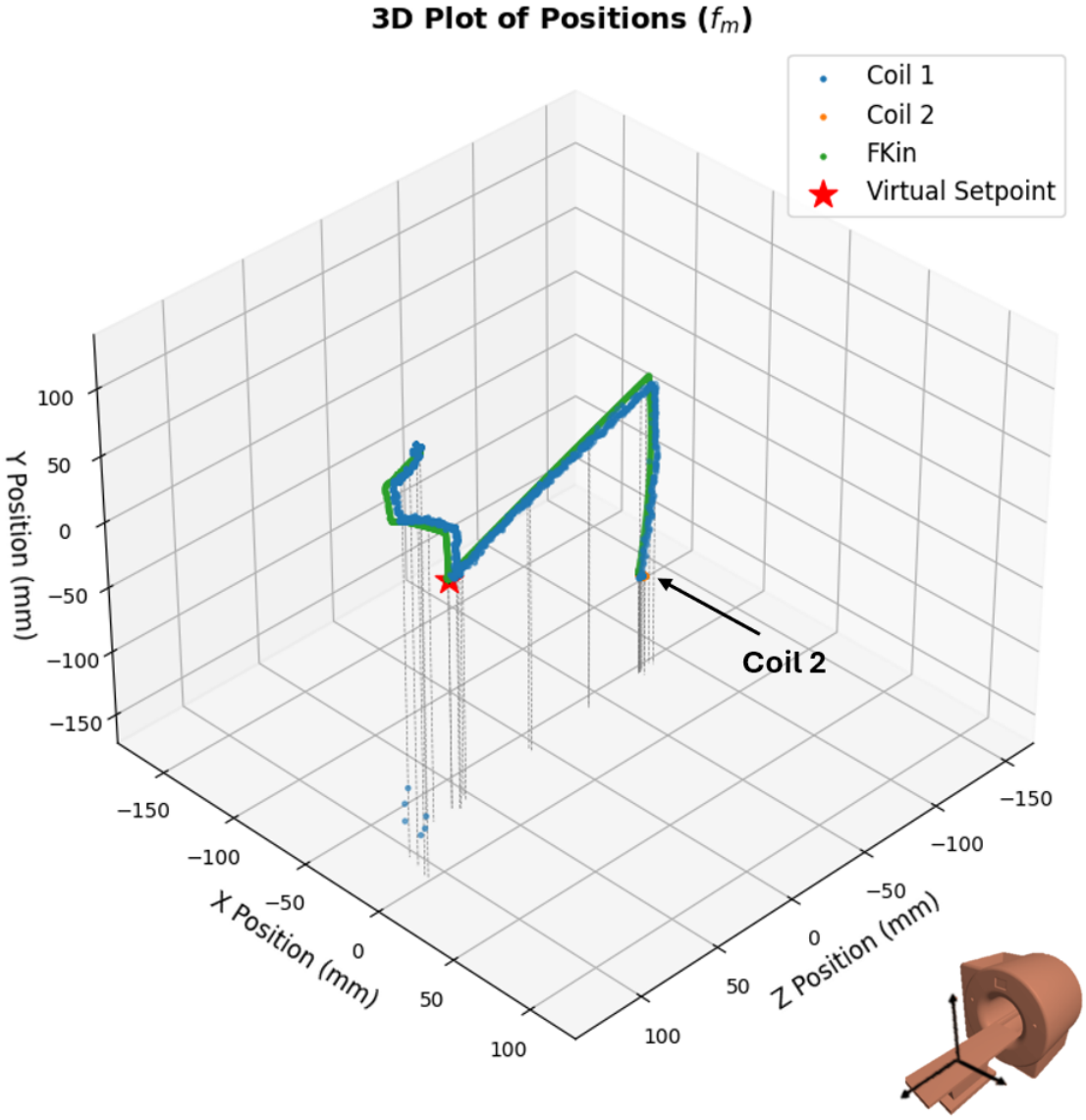

Figure 4.9: Positions of the surrogate needle tip (C1), the anatomical surrogate (C2) and the forward kinematic prediction of the surrogate needle tip location. The needle is first driven towards the virtual setpoint and additionally driven towards the position of the anatomical surrogate shown in a 3D plot. Grey vertical lines indicate the height and position of the trajectories.

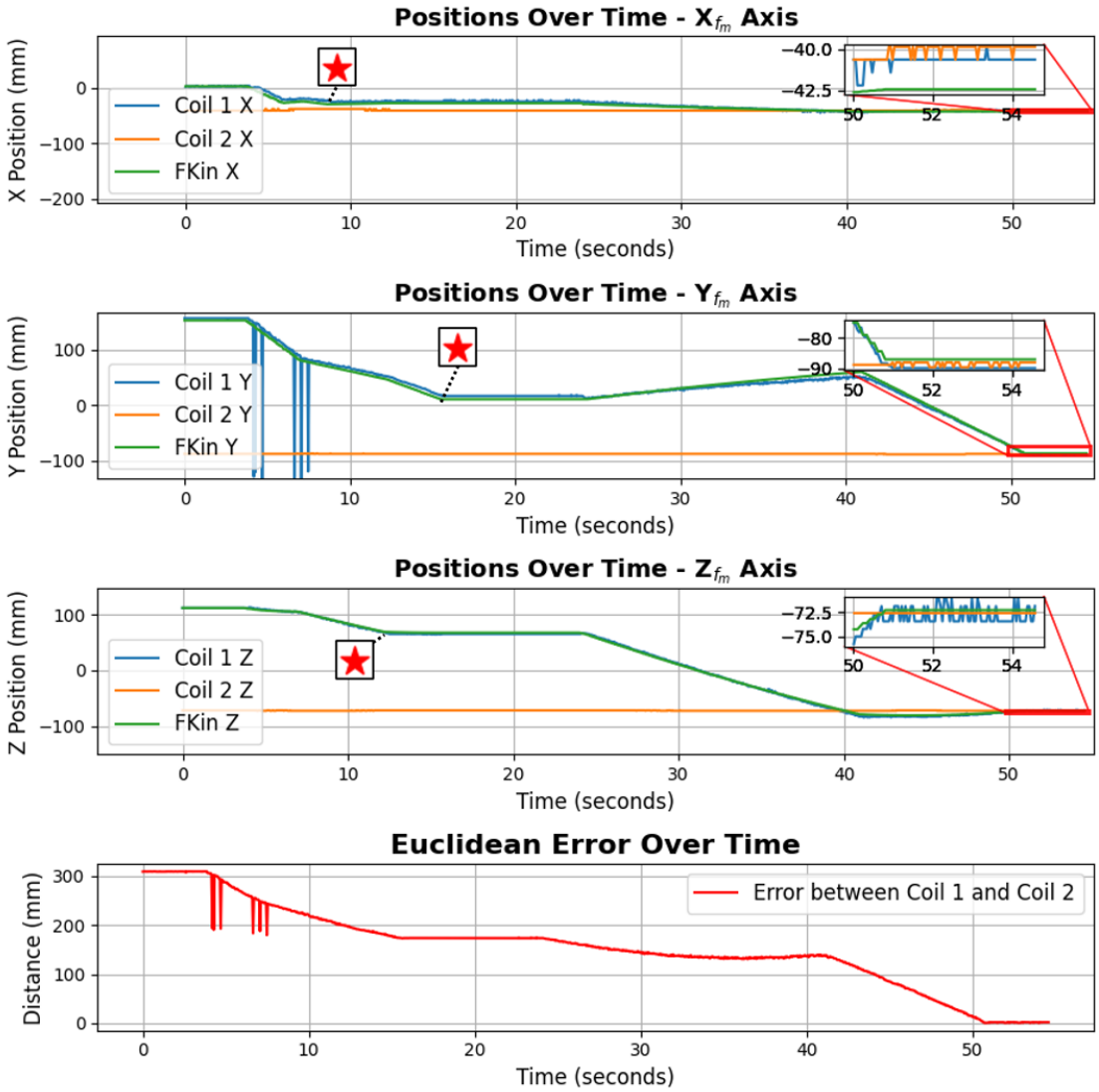

Figure 4.10: Positions of the surrogate needle tip (C1), the anatomical surrogate (C2) and the forward kinematic prediction of the surrogate needle tip location. The needle is first driven towards the virtual setpoint, indicated by the red star and subsequently driven toward the position of the anatomical surrogate. The data is shown for each axis, including a 5-second zoom-in to evaluate data consistency. The results indicate some fluctuations in the acquired position along the path. At the end of the induced movement, the coils were positioned near each other. In the y_{f_m}-axis outliers are observed, appearing as vertical stripes, with some isolated occurrences, such as around t=5 seconds.

Table 4.1: Euclidean position errors of static performance test (in mm)

Measurement	**Virtual Target (mm)**	**Anatomical Surrogate (C2) (mm)**
1	8.03 ± 1.35	2.77 ± 1.35
2	7.09 ± 1.35	1.16 ± 1.35
3	8.19 ± 1.35	4.56 ± 1.35
Mean	**7.77 ± 0.78**	**2.83 ± 0.78**

4.2.2 Dynamic performance test

The position data for the surrogate needle tip, tracked by RF microcoil 1, following a virtual setpoint moving in a straight line along the x_{f_m}-axis with a sinusoidal pattern over time at 0.1 Hz (Figure 4.13), suggests a small delay between the setpoint of the needle tip and the actual measured needle tip location. However, no noticeable increase in delay is observed for higher frequencies of 0.2 Hz (Figure 4.12) and 0.33 Hz (Figure 4.13. The data shows that the kinematic model incorporates movement in the Y_{f_m} and Z_{f_m} axes to follow the setpoint along the x_{f_m}-direction. The mean Euclidean position error for these measurements is presented in Table 4.2.

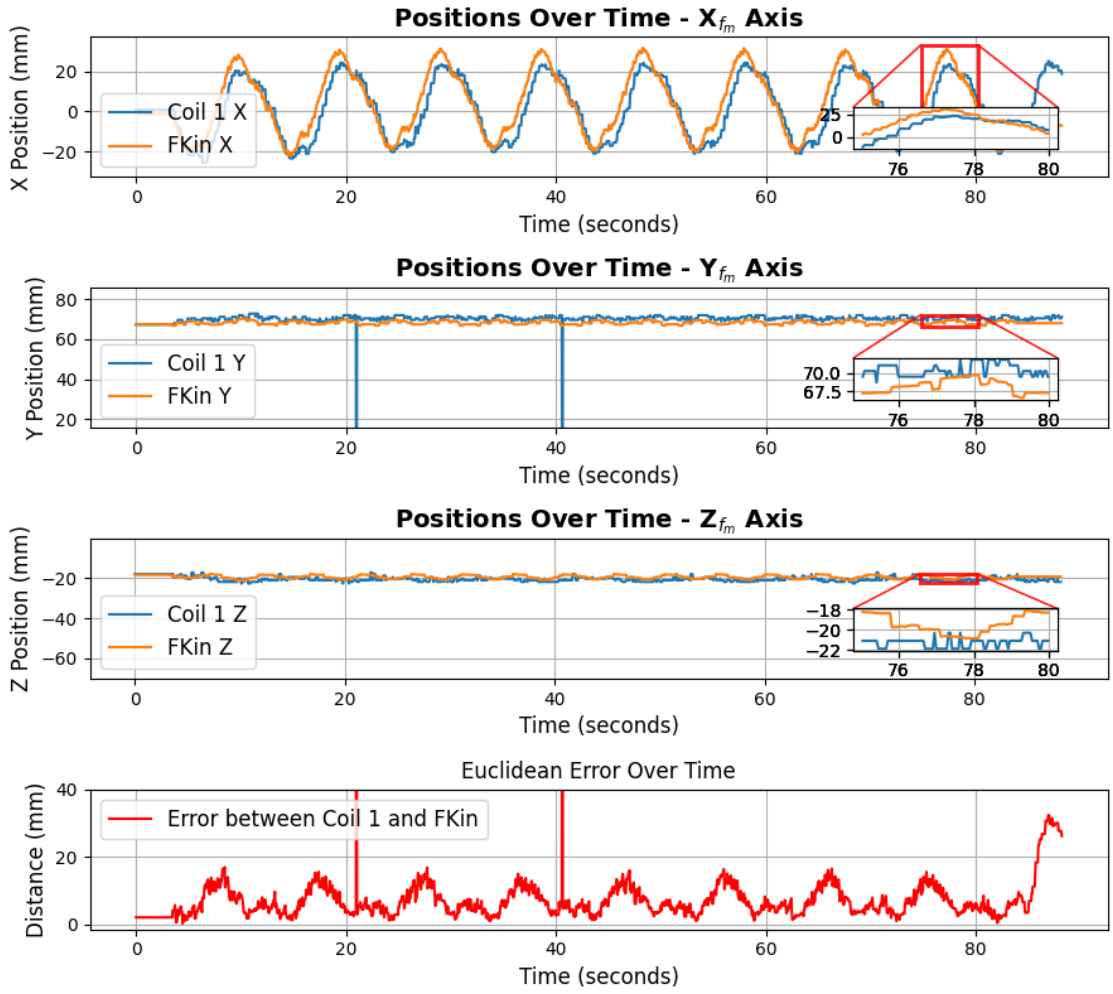

Figure 4.11: Positions of the surrogate needle tip (C1) and the forward kinematic prediction of the surrogate needle tip location, following a virtual setpoint in the x_{f_m}-direction at 0.1 Hz, with an amplitude of 30 mm. The data is shown for each axis, including a 5-second zoom-in to evaluate data consistency. The results indicate that C1 follows the prediction but offsets from the smaller adjustments induced by the kinematic model. Additionally, some fluctuations in the acquired position along the path are observed. In the y_{f_m}-axis outliers appear as vertical stripes, with isolated occurrences, such as around t=21 seconds. These outliers are also present in the Euclidean error plot, which further shows that the error is maximal slightly before reaching the most positive position in x_{f_m}-direction and minimal when the direction of the movement shifts, allowing the kinematic prediction to catch up with the measured location of C1.

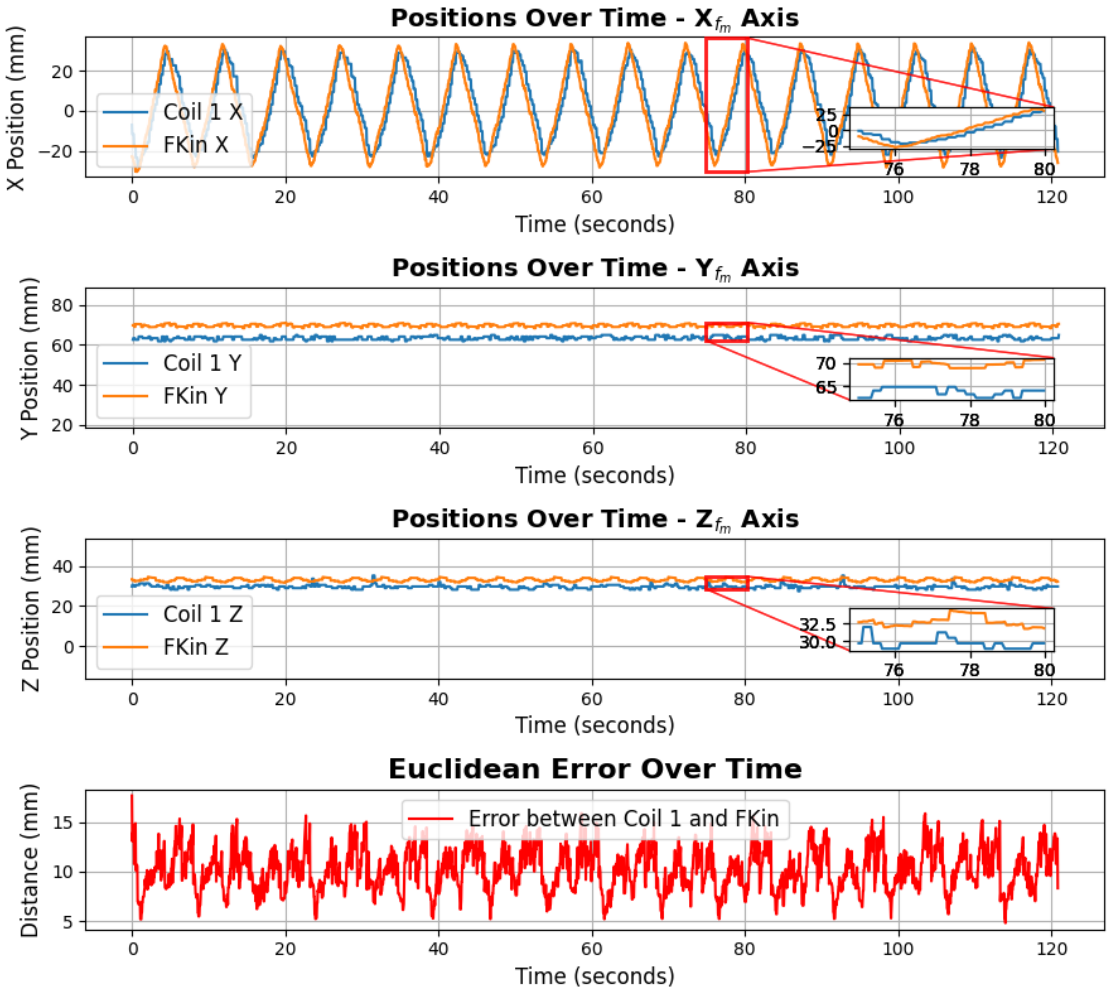

Figure 4.12: Positions of the surrogate needle tip (C1) and the forward kinematic prediction of the surrogate needle tip location, following a virtual setpoint in the x_{f_m}-direction at 0.2 Hz, with an amplitude of 30 mm. The data is shown for each axis, including a 5-second zoom-in to evaluate data consistency. The results indicate that C1 follows the prediction but offsets from the smaller adjustments induced by the kinematic model. In the y_{f_m}-direction an offset of approximately 5 mm is seen for the complete measurement. Additionally, some fluctuations in the acquired position along the path are observed. The Euclidean error plot shows that the error oscillates within a domain of 10 mm during the follow-trajectory.

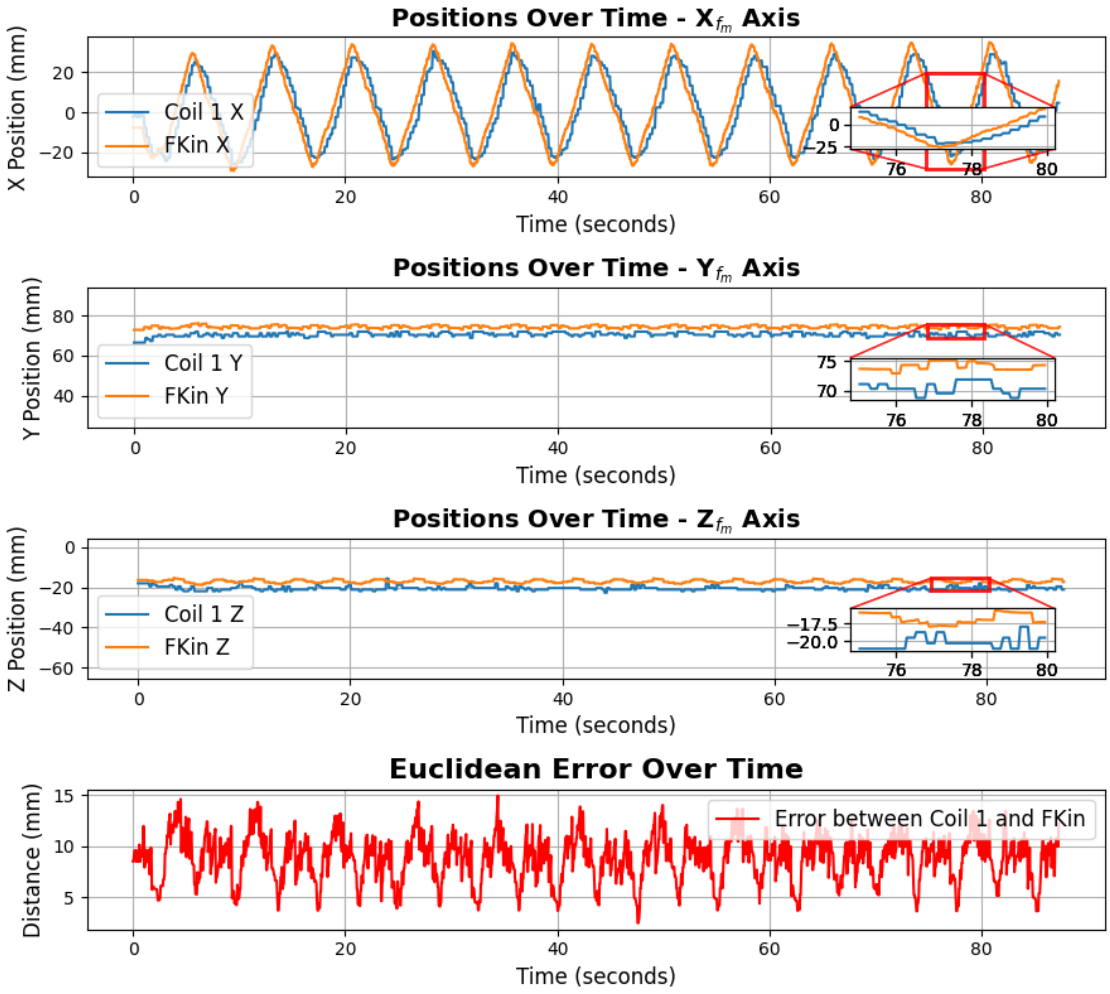

Figure 4.13: Positions of the surrogate needle tip (C1) and the forward kinematic prediction of the surrogate needle tip location, following a virtual setpoint in the x_{f_m}-direction at 0.33 Hz, with an amplitude of 30 mm. The data is shown for each axis, including a 5-second zoom-in to evaluate data consistency. The results indicate that C1 follows the prediction but offsets from the smaller adjustments induced by the kinematic model. In the y_{f_m}-direction an offset of approximately 4 mm is seen for the complete measurement. Additionally, some fluctuations in the acquired position along the path are observed. The Euclidean error plot shows that the error is maximal slightly before reaching the most positive position in x_{f_m}-direction and minimal when the direction of the movement shifts, allowing the kinematic prediction to catch up with the measured location of C1. This plot also indicates that the error oscillates within a domain of 10 mm during the follow-trajectory.

Table 4.2: Mean Euclidean position errors measured during dynamic performance testing, following a virtual sinusoidal moving target (in mm)

Frequency (Hz)	Virtual Target (mm)
0.10	7.27 ± 0.03
0.20	10.13 ± 0.03
0.33	8.71 ± 0.03

The measurements where MAMRI was driven to follow the dynamic anatomical surrogate (C2) moving with a frequency of 0.12 Hz (Figure 4.14) show the path towards the target. When the live following was enabled, it can be seen that MAMRI tried to follow the sinusoidal curve of the target. Delays are seen, where MAMRI already moves to the opposite position before reaching the 'extreme' positions of the target. This effect increases on the z_{f_m}-axis for the faster frequencies of 0.15 Hz (Figure 4.15) and 0.20 Hz (Figure 4.16). Table 4.3 shows that the Euclidean position error also increases for the higher frequencies.

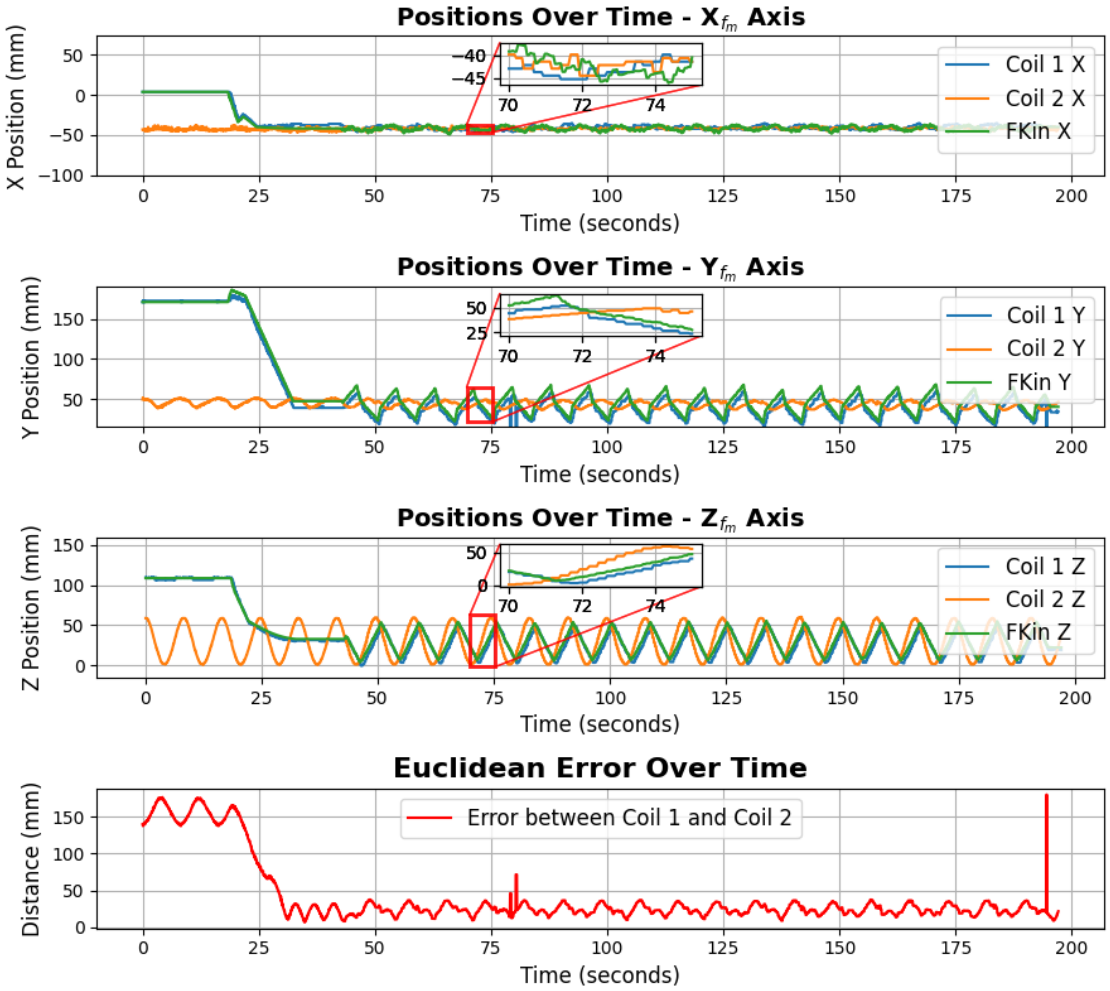

Figure 4.14: Position of the surrogate needle tip (C1) following the dynamic anatomical surrogate (C2) moving at 0.12 Hz with an amplitude of 30 mm. The data is shown for each axis, including a 5-second zoom-in to evaluate data consistency. The results indicate that the location of C1 follows the forward kinematic prediction position with small offsets. The position data of C1 and the forward kinematic prediction show an oscillation on the y_{f_m}-axis with an amplitude being approximately twice the amplitude of the movement of C2 on this axis. A delay is observed in the needle position following the target. Additionally, some fluctuations in the acquired position along the path are observed. The Euclidean error plot indicates that the error oscillates during the follow-trajectory.

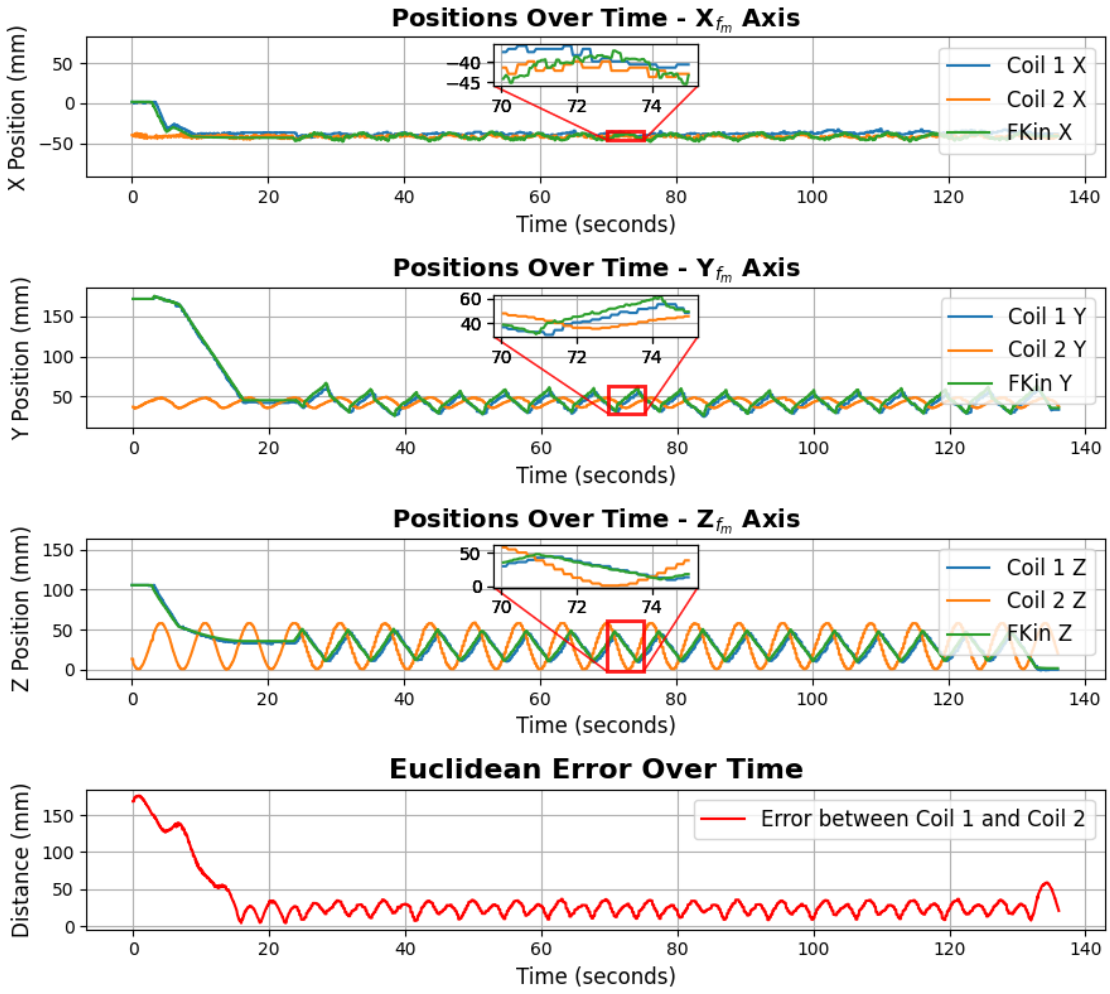

Figure 4.15: Position of the surrogate needle tip (C1) following the dynamic anatomical surrogate (C2) moving at 0.15 Hz with an amplitude of 30 mm. The data is shown for each axis, including a 5-second zoom-in to evaluate data consistency. The results indicate that the location C1 follows the forward kinematic prediction position with small offsets. A delay is observed in the needle position following the target. Additionally, some fluctuations in the acquired position along the path are observed. The Euclidean error plot indicates that the error oscillates during the follow-trajectory.

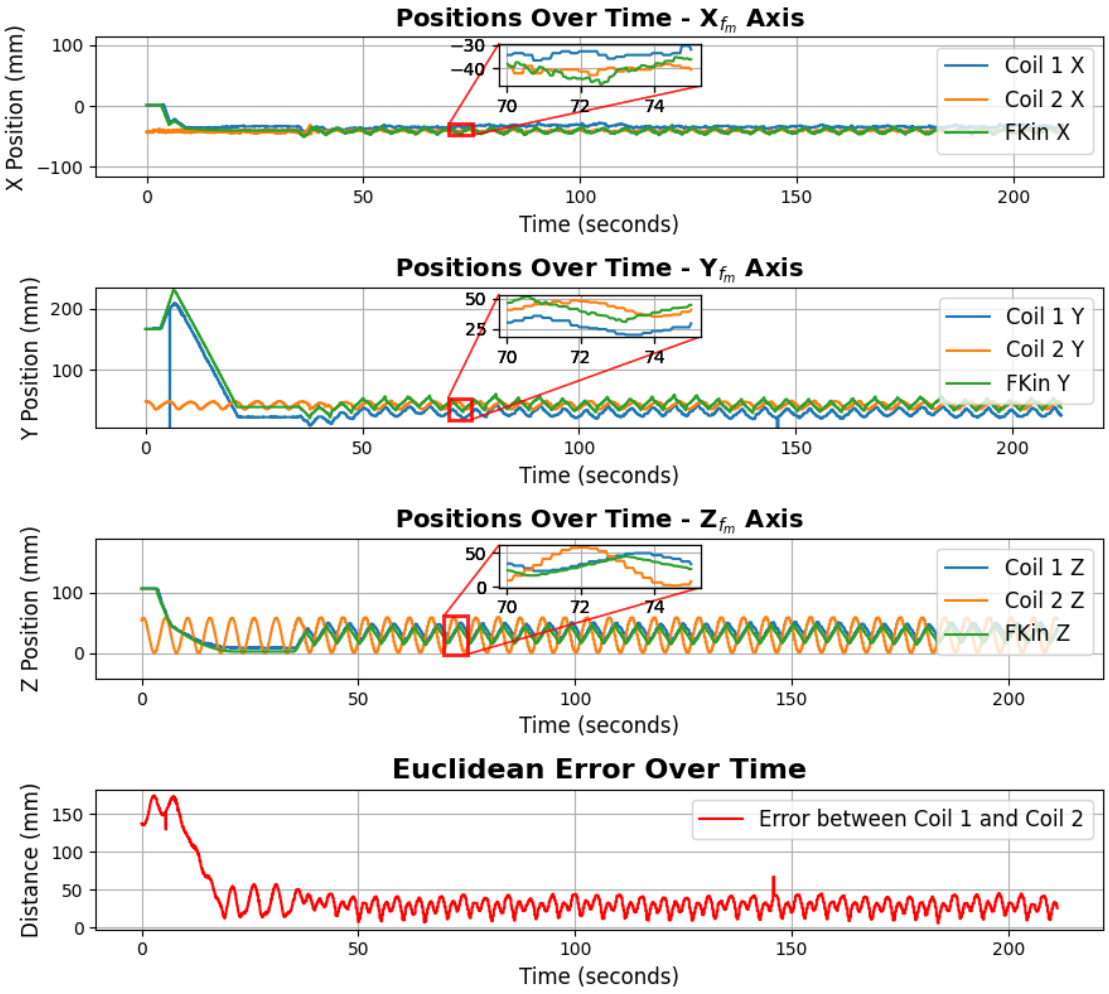

Figure 4.16: Position of the surrogate needle tip (C1) following the dynamic anatomical surrogate (C2) moving at 0.20 Hz with an amplitude of 30 mm. The data is shown for each axis, including a 5-second zoom-in to evaluate data consistency. The results indicate that the location C1 follows the forward kinematic prediction position with small offsets. In the y_{f_m}-direction an offset of approximately 10 mm is seen between the prediction and C1 for the complete measurement. A delay is observed in the needle position following the target. Additionally, some fluctuations in the acquired position along the path are observed. The Euclidean error plot indicates that the error oscillates during the follow-trajectory.

Table 4.3: Mean Euclidean errors measured during dynamic performance testing, following RF microcoil 2 (in mm)

Frequency (Hz)	Anatomical Surrogate (C2) (mm)
0.12	24.15 ± 0.02
0.15	24.49 ± 0.03
0.20	28.66 ± 0.02

5 Discussion

Within this chapter, the findings and results found in this research will be evaluated concerning the central research question of this thesis: **How can active MR-tracking be used to characterize and enhance the performance of the 6-DOF pneumatic MR-safe manipulator arm for MRI (MAMRI)?**. First, the design and control will be evaluated, followed by an assessment of the RF microcoil tracking and the MAMRI performance.

5.1 Design and control

The pneumatically driven needle guide (Figure 3.2) was designed to be compact and capable of actuating a 200 mm needle. However, the design of the rack-motor combination used in this system limits the usable injection length along the needle. A shorter rack in the current design would increase the free injection length but reduce the possible action length.

For the purposes of this research, where a surrogate needle was used, this limitation in the end-effector design did not affect the study's outcomes. However, for future implementations of MAMRI with full usable injection length and actuation, a redesign of the end-effector is recommended. Possible solutions include using a flexible belt mechanism or attaching the pneumatic motor directly to the needle rather than to the end-effector.

The collision avoidance protocol described in Section 3.4.3 was based on a sphere defined around the end-effector. Kinematic solutions where the sphere overlapped with the bore were considered too close and were excluded from being passed to the controller for actuation. This approach was straightforward to implement and provided a consistent safety margin regardless of the end-effector's orientation.

However, the safety margin could be reduced for specific end-effector orientations, allowing MAMRI to operate closer to the bore wall. For the measurements conducted in this research, such adjustments were unnecessary. Nevertheless, for future implementations of MAMRI, it is recommended to extend the control model with a more advanced safety protocol. This enhancement would improve the reachable workspace while maintaining safe operation. Additionally, when working with a volume inside the scanner, such as a patient, it is recommended to also add a protocol to avoid collisions with this volume, except for the intervention itself. Such a protocol could be based, for instance, on a rough 3D scan of this volume inside the MRI.

5.2 RF microcoil tracking

The tracking sequence used to localize the RF microcoils within the scanner performed as expected, and no issues were encountered. However, developing a custom sequence could offer advantages. A custom sequence would provide greater control over the received signal and allow for the exploration of multiple scan parameters to enhance tracking performance.

Additionally, in this setup, the number of samples per axis was limited to 640 due to software constraints. In previous experience it was seen that this number could be increased. A higher number of samples would reduce the spatial distance between sample points while the Field of View (FoV) remains large enough to track the coils across the entire bore diameter. This adjustment would improve the spatial accuracy of active tracking.

Within the results section (Section 4.1) small oscillations were seen in the location of the microcoils, these oscillations are 0.78 mm, which corresponds to the spatial resolution. Therefore, a possible explanation for these oscillations is the real position of the specific RF microcoil being exactly in between the defined sampling points. As a result, a small change in the signal will cause fluctuation in the observed position. This effect could be reduced by increasing the spatial resolution. For larger fluctuations, as shown in the z_{fm} plot of Figure 4.6, it can be

considered to use interpolation, postprocessing of the projection data, or implementing preamplifiers in the RF microcoils to enhance the signal to noise ratio (SNR) to improve the accuracy and consistency of the acquired RF microcoil locations. Besides, for the measurements where the RF micro-coils are moved, vibrations in the setups can also cause fluctuations in the acquired locations.

Additionally, it was seen that when the solenoid of the RF microcoil was positioned parallel to the main magnetic field of the MRI (B_0) it was not possible to accurately localize the coil inside the scanner. This behaviour was also seen in other studies [32]. A possible explanation could be that there is no net magnetization along the coil when being parallel to B_0, with minimal change in magnetic flux, no significant signal can be detected of the coil [33].

However, this limitation can be overcome by carefully positioning the RF microcoils or by using two perpendicularly aligned coils. For the measurements whereas the performance of MAMRI was evaluated, the micro-coil was always positioned perpendicular to B_0 so that the orientation dependence of the RF microcoils did not affect the results. Additionally, it would be recommended to investigate if the cut-off angles observed, where the location signal is lost, differ for different positions along the bore due to possible inhomogeneities of the field.

When the RF microcoil was actuated outside the Field of View, no constant location was observed as shown in Section 4.1. This can be explained by the MRI system, which uses a predefined FoV to excite and spatially encode signals from objects within this region. When the RF microcoil moves outside the FoV, no spatially encoded signal is received along the corresponding axis. As a result, only background noise is detected, causing the acquired location information to fluctuate in accordance with peaks in the Gaussian background noise.

5.3 MAMRI performance

Within Figure 4.7, it is shown that the needle was moved slightly oblique compared to its intended direction, this can be caused by inappropriate calibration of the robot or by missing steps over time. This results in a mismatch between the kinematic model and the real position of MAMRI. This can also be the cause of the offset seen in Figures 4.12, 4.13 and 4.16. The observed Euclidean position errors can also be negatively influenced by these phenomena.

Overall, it is observed that the position of the surrogate needle tip and the forward kinematic prediction line up with some fluctuating distance of several millimetres in between. These errors can be minimalized by improving the calibration and homing process of MAMRI, for instance, by using optical encoders for homing or by minimizing the possibility of missed steps further by improving the airtightness of MAMRI.

However, Figures 4.11, 4.12, 4.13 and Table 4.2 do not indicate a relation between increase of this error and following setpoints moving with a higher frequency. The error is also not increasing over time, indicating that there was no significant amount of steps missed during these measurements. Besides, when the Euclidean position errors between the static virtual target and the moving virtual target are compared, as described in Table 4.1 and 4.2, comparable errors are observed. This suggests that the error is mainly induced by inappropriate calibration of MAMRI.

Additionally, an error between the acquired needle location and the kinematic model could be continuously downsized by closed-loop control with the MRI data, being also one of the future work proposals.

Table 4.1 shows a mean accuracy of 2.83 $\pm$ 0.78 mm for targeting a static lesion, while other 6-DOF interventional MRI robots show an accuracy ranging from 2.55 mm to 10 mm [17]. This shows the potential of the MAMRI system to compete with the current developed systems described in research, when the mismatch between the kinematic model and the real location of

the needle can be further downsized as described above, the system should, in theory, have the potential to perform better than the systems described.

However, it should be noted that the measurements of the accuracy of MAMRI were performed in the air without the influence of surrounding tissue or volumes interfering with the needle and its position. This may lead to an overly optimistic accuracy assessment. However, if tissue interactions cause greater deviations in needle position compared to the setpoint, the implementation of closed-loop control with the MRI or MRI-safe pressure sensors could potentially minimize these offsets.

For the dynamic targeting accuracy no concrete comparison with available systems in research could be made. However, based on the kinematic evaluation executed within this research, it is considered that improvements in this accuracy should and could be made, as will be described below.

Based on the data shown in Figures 4.11, 4.12 and 4.13, it is observed that while MAMRI follows a sinusoidal virtual setpoint along the x_{fm}-axis, small oscillations occur in other directions. This behaviour is influenced by the design of the kinematic model. In this setup, all motors were driven at the maximum speed possible within the MRI experiment. As a result, motors with fewer steps to reach their setpoint complete their movement faster than those requiring more steps. For example, a motor taking two steps reaches its setpoint earlier than another needing 60 steps to satisfy the configuration for a specific needle tip position.

This mismatch causes the end-effector to begin moving toward the next setpoint before it has fully reached the current one, introducing lag and leading to oscillations in directions other than the induced path. This also explains the sawtooth pattern observed in the movement along the x_{fm}-axis. The end-effector joints attempt to keep up with the continuously adjusted setpoint but reach their setpoint near the peak of the sinusoidal curve, where the target's speed is slower.

This behaviour could be limited by scaling the step frequency of each motor at every setpoint to match the motor that requires the most steps. This adjustment would ensure a smooth movement, with all joints reaching their setpoints simultaneously.

However, a significant drawback of this approach is the overall reduction in MAMRI's speed. Slower joints would delay the faster ones, making it more difficult to follow fast-moving targets and increasing the lag between the robot and the target. The approach chosen in this research prioritizes the fastest possible tracking of a target with minimal lag.

In a clinical setting, such as tracking a moving liver lesion due to respiration, a faster alignment of the needle guide is crucial, particularly during a breath-hold procedure. In these scenarios, the faster approach ensures that the needle guide aligns with the target's position more quickly, even if slight oscillations are present, compared to a slower, smoother approach.

Within this research a surrogate anatomy was used to omit image processing speed and real-time image tracking quality limiting the real-time assessment of the kinematic model of MAMRI. However, for future implementation of MAMRI with real-time 3D tracking of a lesion, an image-based tracking algorithm should be developed.

To evaluate MAMRI's kinematic performance on a system level, without depending on the kinematic model to predict the needle position based on an RF microcoil or marker on the arm, the RF microcoil was placed on the 'needle' tip in this research. However, the next step for follow-up research would be implementing an RF microcoil on the arm when the kinematic model is adopted as reliable.

To combine the image-based tracking of the lesion and the RF microcoil tracking of the arm the use of a generalized autocalibrating parallel acquisitions algorithm (GRAPPA) combined with an active tracking sequence [34] could, for instance, be considered.

6 Conclusions and Recommendations

This research marked the initial steps in implementing real-time MRI active tracking using RF microcoils to enhance MR-guided abdominal biopsies, within this chapter, conclusions will be stated to answer the main research question: '**How can active MR-tracking be used to characterize and enhance the performance of the 6-DOF pneumatic MR-safe manipulator arm for MRI (MAMRI)?**'. Additionally, recommendations will be formulated for follow-up research to further enhance MR-guided biopsies.

6.1 Conclusions

A tailored version of MAMRI, a 6-DOF Manipulator Arm for MRI actuated by pneumatic stepper motors, was employed in multiple MRI experiments utilizing a fully functional kinematic model. Additionally, a platform was developed to facilitate easy switching between end-effectors, including needle guides for various needle formats and a pneumatically actuated needle guide for remote-controlled interventions, enabling remote needle injections with various speeds.

Active tracking was successfully utilized to localize RF microcoils within the MRI environment. These coils served as surrogates for the needle and anatomical structures. The surrogate needle location was effectively used to calibrate MAMRI to the MRI coordinate frame, and collision protocols were implemented to prevent collisions with the bore and MRI table.

MAMRI was successfully controlled via the developed GUI. Active tracking was used to assess the kinematic performance of MAMRI.

The kinematic assessment indicates that MAMRI did not miss a significant amount of steps during actuation and demonstrates the potential to compete in accuracy with other state-of-the-art 6-DOF robotic systems for MRI-guided interventions. The system is capable of following dynamic targets. However, the actuation speed and possibly approach have to be improved to enhance the dynamic accuracy.

In general, the kinematic model can be used to successfully evaluate the performance of MAMRI and predicted the location of the needle with a reasonably small offset, which potentially be minimized in future research. These findings suggest that integrating MAMRI with active tracking offers significant potential advantages for MR-guided interventions, potentially enhancing the biopsy needle placement accuracy in dynamic abdominal lesions, clinical workflow and ultimately leading to better clinical outcomes. This could contribute to improved abdominal cancer diagnosis.

6.2 Recommendations

In this research, MAMRI was actuated using 24 pneumatic tubes (4 tubes per pneumatic motor). However, by connecting tubes to multiple motors and employing a more advanced sequenced method for actuating the pneumatic valves, it may be possible to reduce the number of tubes to 12 (1 tube per 2 motors). This modification has the potential to make the system more compact and flexible by reducing the space occupied by pneumatic tubes.

Additionally, for abdominal interventions, it would be valuable to incorporate a Remote Center of Motion (RCM). This feature could enable a rotation point at the abdominal wall, allowing pivoting around this point to facilitate movement within the abdominal cavity, as seen in trocar-based interventions. In the current kinematic model, preliminary steps have been taken to implement an RCM, and the existing code can generate an RCM. However, optimization is needed for full functionality in the control algorithm. For follow-up research, it is recom-

mended to further develop and optimize the RCM functionality to enhance the versatility and clinical applicability of MAMRI.

A Abbreviations

Table A.1: List of abbreviations used in this thesis.

Abbreviation	Definition
bSSFP	Balanced Steady State Free Precession
CNN	Convolutional Neural Network
CT	Computer Tomography
DOF	Degrees of Freedom
FoV	Field of View
FPS	Frames Per Second
GRASP	Golden-angle Radial Sparse Parallel
MAMRI	Manipulator Arm for MRI
MOTUS	Motion from Undersampled Signal
MR	Magnetic Resonance
MRI	Magnetic Resonance Imaging
NMR	Nuclear Magnetic Resonance
PLA	Polyacrylate
RF	Radio Frequency
SNR	Signal to noise ratio
SS-FSE	Single Shot Fast Spin Echo
US	Ultrasound

References

[1] *Global cancer burden growing, amidst mounting need for services*. [Online]. Available: https://www.who.int/news/item/01-02-2024-global-cancer-burden-growing--amidst-mounting-need-for-services.

[2] *Cancer Today*. [Online]. Available: https://gco.iarc.fr/today/en/dataviz/pie?mode=cancer&group_populations=1.

[3] N. I. Sainani, R. S. Arellano, P. B. Shyn, D. A. Gervais, P. R. Mueller and S. G. Silverman, 'The challenging image-guided abdominal mass biopsy: Established and emerging techniques 'if you can see it, you can biopsy it'', *Abdominal Imaging*, vol. 38, no. 4, pp. 672–696, Aug. 2013, ISSN: 09428925. DOI: 10.1007/S00261-013-9980-0/FIGURES/31. [Online]. Available: https://link.springer.com/article/10.1007/s00261-013-9980-0.

[4] V. F. Schmidt, O. Öcal, V. Walther *et al.*, 'Clinical benefits of MRI-guided freehand biopsy of small focal liver lesions in comparison to CT guidance.', *European radiology*, vol. 34, no. 9, pp. 5507–5516, Sep. 2024, ISSN: 1432-1084. DOI: 10.1007/s00330-024-10623-9.

[5] *MAGNETOM Symphony, A Tim System 1.5T eco - used MRI machine - Siemens Healthineers USA*. [Online]. Available: https://www.siemens-healthineers.com/en-us/refurbished-systems-medical-imaging-and-therapy/ecoline-refurbished-systems/magnetic-resoncance-imaging-ecoline/magnetom-symphony-tim-eco.

[6] *MRI Systems: dedicated and whole body open magnetic resonance - Esaote*. [Online]. Available: https://www2.esaote.com/magnetic-resonance/magnetic-resonance-systems/.

[7] *Brain Surgery | GE News*. [Online]. Available: https://www.ge.com/news/taxonomy/term/1168.

[8] *MAGNETOM Aera - Siemens Healthineers USA*. [Online]. Available: https://www.siemens-healthineers.com/en-us/magnetic-resonance-imaging/0-35-to-1-5t-mri-scanner/magnetom-aera.

[9] C. R. Weiss, S. G. Nour and J. S. Lewin, 'MR-guided biopsy: A review of current techniques and applications', *Journal of Magnetic Resonance Imaging*, vol. 27, no. 2, pp. 311–325, Feb. 2008, ISSN: 1522-2586. DOI: 10.1002/JMRI.21270. [Online]. Available: https://onlinelibrary.wiley.com/doi/full/10.1002/jmri.21270.

[10] H. Busse, T. Kahn and M. Moche, 'Techniques for Interventional MRI Guidance in Closed-Bore Systems', *Topics in Magnetic Resonance Imaging*, vol. 27, no. 1, pp. 9–18, Feb. 2018, ISSN: 15361004. DOI: 10.1097/RMR.0000000000000150. [Online]. Available: https://journals.lww.com/topicsinmri/fulltext/2018/02000/techniques_for_interventional_mri_guidance_in.5.aspx.

[11] H. Ranjan, M. Van Hilten, V. Groenhuis *et al.*, 'Sunram 7: An MR Safe Robotic System for Breast Biopsy', *IEEE International Conference on Intelligent Robots and Systems*, pp. 10 281–10 288, 2023, ISSN: 21530866. DOI: 10.1109/IROS55552.2023.10342425.

[12] P. Moreira, G. Van De Steeg, T. Krabben *et al.*, 'The MIRIAM Robot: A Novel Robotic System for MR-Guided Needle Insertion in the Prostate', *Journal of Medical Robotics Research*, DOI: 10.1142/S2424905X17500064. [Online]. Available: http://www.worldscientific.com/worldscinet/jmrr.

[13] A. Melzer, B. Gutmann, T. Remmele *et al.*, 'INNOMOTION for percutaneous image-guided interventions', *IEEE Engineering in Medicine and Biology Magazine*, vol. 27, no. 3, pp. 66–73, May 2008, ISSN: 07395175. DOI: 10.1109/EMB.2007.910274.

[14] A. Reichert, M. Bock, M. Vogele and A. J. Krafft, 'Gantrymate: A modular mr-compatible assistance system for mr-guided needle interventions', *Tomography*, vol. 5, no. 2, pp. 266–273, Jun. 2019, ISSN: 2379139X. DOI: 10.18383/j.tom.2019.00007.

[15] P. A. W. G. Carvalho, C. J. Nycz, K. Y. Gandomi and G. S. Fischer, 'Demonstration and Experimental Validation of Plastic-Encased Resonant Ultrasonic Piezoelectric Actuator for Magnetic Resonance Imaging-Guided Surgical Robots', *Journal of engineering and science in medical diagnostics and therapy*, vol. 3, no. 1, p. 011 002, Feb. 2019, ISSN: 2572-7958. DOI: 10.1115/1.4044609. [Online]. Available: https://pmc.ncbi.nlm.nih.gov/articles/PMC7376759/.

[16] V. Groenhuis and S. Stramigioli, 'Rapid Prototyping High-Performance MR Safe Pneumatic Stepper Motors', *IEEE/ASME Transactions on Mechatronics*, vol. 23, no. 4, pp. 1843–1853, Aug. 2018, ISSN: 10834435. DOI: 10.1109/TMECH.2018.2840682.

[17] S. Huang, C. Lou, Y. Zhou *et al.*, 'Med-X MRI-guided robot intervention-current state-of-the-art and new challenges', vol. 1, p. 3, DOI: 10.1007/s44258-023-00003-1. [Online]. Available: https://doi.org/10.1007/s44258-023-00003-1.

[18] K. S. Nayak, Y. Lim, A. E. Campbell-Washburn and J. Steeden, 'Real-Time Magnetic Resonance Imaging', *Journal of magnetic resonance imaging : JMRI*, vol. 55, no. 1, pp. 81–99, Jan. 2022, ISSN: 1522-2586. DOI: 10.1002/JMRI.27411. [Online]. Available: https://pubmed.ncbi.nlm.nih.gov/33295674/.

[19] H. H. Wu, P. T. Gurney, B. S. Hu, D. G. Nishimura and M. V. Mcconnell, 'Free-Breathing Multiphase Whole-Heart Coronary MR Angiography Using Image-Based Navigators and Three-Dimensional Cones Imaging', *Magnetic Resonance in Medicine*, vol. 69, pp. 1083–1093, 2013. DOI: 10.1002/mrm.24346. [Online]. Available: https://onlinelibrary.wiley.com/doi/10.1002/mrm.24346.

[20] X. Li, A. S. Young, S. S. Raman *et al.*, 'Automatic needle tracking using Mask R-CNN for MRI-guided percutaneous interventions', *International Journal of Computer Assisted Radiology and Surgery*, vol. 15, no. 10, pp. 1673–1684, Oct. 2020, ISSN: 18616429. DOI: 10.1007/S11548-020-02226-8/FIGURES/7. [Online]. Available: https://link.springer.com/article/10.1007/s11548-020-02226-8.

[21] S. E. Song, N. B. Cho, I. I. Iordachita, P. Guion, G. Fichtinger and L. L. Whitcomb, 'A study of needle image artifact localization in confirmation imaging of MRI-guided robotic prostate biopsy', *Proceedings - IEEE International Conference on Robotics and Automation*, pp. 4834–4839, 2011, ISSN: 10504729. DOI: 10.1109/ICRA.2011.5980309.

[22] N. R. F Huttinga, T. Bruijnen, C. A. T van den Berg, A. Sbrizzi and C. R. Niek F Huttinga, 'Nonrigid 3D motion estimation at high temporal resolution from prospectively undersampled k-space data using low-rank MR-MOTUS for Magnetic Resonance in Medicine', 2020. DOI: 10.1002/mrm.28562. [Online]. Available: https://onlinelibrary.wiley.com/doi/10.1002/mrm.28562.

[23] L. Feng, 'Live-view 4D GRASP MRI: A framework for robust real-time respiratory motion tracking with a sub-second imaging latency', 2023. DOI: 10.1002/mrm.29700. [Online]. Available: https://onlinelibrary.wiley.com/doi/10.1002/mrm.29700.

[24] C. L. Dumoulin, S. P. Souza and R. D. Darrow, 'Real-time position monitoring of invasive devices using magnetic resonance', *Magnetic Resonance in Medicine*, vol. 29, no. 3, pp. 411–415, 1993, ISSN: 15222594. DOI: 10.1002/mrm.1910290322.

[25] B. R. Daniels, R. Pratt, R. Giaquinto and C. Dumoulin, 'Optimizing accuracy and precision of micro-coil localization in active-MR tracking', *Magnetic Resonance Imaging*, vol. 34, no. 3, pp. 289–297, Apr. 2016, ISSN: 18735894. DOI: 10.1016/j.mri.2015.11.005.

[26] V. Groenhuis, M. Bac and S. Stramigioli, 'Controlling an MR Safe Robot Arm with Six Pneumatic Stepper Motors using Eight Tubes', 2024.

[27] T. T. Trang, T. L. Pham, Q. N. Yin, Q. W. Wang, Y. M. Hu and W. G. Li, 'Design Harmonic Drive for Application in Robot Joint', *2022 International Conference on Mechanical and Electronics Engineering, ICMEE 2022*, pp. 106–113, 2022. DOI: 10.1109/ICMEE56406.2022.10093325.

[28] R. Sneep, 'CREATING A MR SAFE ROBOTIC PLATFORM', Tech. Rep.

[29] B. Bloemendaal, 'Accuracy and Precision of MR-based Active Tracking using Receiver Micro-coils', Tech. Rep., 2022.

[30] J. L. Prince and J. M. Links, *Medical Imaging Signals and Systems*. Pearson, 2015, ISBN: 9780132145183. [Online]. Available: https://books.google.nl/books?id=HHrangEACAAJ.

[31] I. Suramo, M. Paivansalo and V. Myllyla, 'Cranio-caudal movements of the liver, pancreas and kidneys in respiration', *Acta radiologica: diagnosis*, vol. 25, no. 2, pp. 129–131, 1984, ISSN: 0567-8056. DOI: 10.1177/028418518402500208. [Online]. Available: https://pubmed.ncbi.nlm.nih.gov/6731017/.

[32] N. Garnov, G. Thörmer, R. Trampel *et al.*, 'Suitability of miniature inductively coupled RF coils as MR-visible markers for clinical purposes', 2011. DOI: 10.1118/1.3655027. [Online]. Available: https://aapm.onlinelibrary.wiley.com/doi/10.1118/1.3655027.

[33] B. Guo, S. Liu, S. Yang, G. Li, J. Li and X. Sun, 'Orthogonal micro-fluxgate with S-shape excitation wire and 3D solenoid detection coil', *Microsystem Technologies*, vol. 21, no. 8, pp. 1579–1586, Aug. 2015, ISSN: 09467076. DOI: 10.1007/S00542-014-2326-1/METRICS. [Online]. Available: https://link.springer.com/article/10.1007/s00542-014-2326-1.

[34] M. Bock, S. Müller, S. Zuehlsdorff *et al.*, 'Active catheter tracking using parallel MRI and real-time image reconstruction', *Magnetic Resonance in Medicine*, vol. 55, no. 6, pp. 1454–1459, 2006, ISSN: 15222594. DOI: 10.1002/mrm.20902.